

High-Performance Dielectric Substrate
Development with Low D_k and D_f for RF and
mm-wave Applications

by
Umut Barış Göğebakan

Submitted to the Graduate School of Engineering and Natural Sciences
in partial fulfillment of
the requirements for the degree of
Master of Science

Sabancı University

Summer, 2021

High-Performance Dielectric Substrate Development with Low D_k and D_f for RF
and mm-wave Applications

Approved by:

[Redacted signature]

[Redacted signature]

[Redacted signature]

[Redacted signature]

[Redacted signature]

Date of Approval:

Aileme...
To my family...

Umut Barış Göğebakan 2021 ©

All Rights Reserved

Acknowledgements

This work was supported by ASELSAN corporation under the Grant EACF-20-02127, “High-Performance Dielectric Substrate Development with Low D_k and D_f for RF and mm-wave at 94 GHz”.

Initially, I would like to express my gratitude to both of my supervisors Prof. Yaşar Gürbüz, and Assoc. Prof. Güllü Kızıldağ Şendur for their precious guidance in my undergraduate and master’s years. I would also like to thank my thesis jury members, Asst. Prof. Melik Yazıcı, Assoc. Prof. Metin Yazgı, and Prof. Bulat Rami for their valuable time to spare in my thesis committee and for their precious comments, advice, and feedback. Additionally, I would like to thank Deniz Anıl, Merve Senem Seven, and Yeşim Menciloğlu for the precious efforts to realize this work in terms of detailed fabrication steps.

I would like to thank to my friends and colleagues at the Sabanci University Microelectronics Research Group (SUMER): Asst. Prof. Ömer Ceylan, Ajten Fejzullahu, Tahsin Alper Özkan, Kaan Veziroğlu, Bahadır Özdöl, Abdurrahman Burak, Kutay Altuntaş, Cengizhan Kana, Cerin Ninan Kunnatharayil, Erkut Gürol, and Ekin Asım Özek, and Melih Taşdelen for their friendship which made the working environment comfortable for me and keep me motivated. I would also like to thank the former members including the former members of SUMER: Mir Hassan Mahmud, Hamza Kandış, and Elif Gül Özkan Arsoy for their support and guidance. I also thank Ali Kasal, the laboratory specialist, for his support and help.

I am grateful to Ezgi Hamamcı, Meltem Ünalın, Azelya Tanrıverdi, Şahin Yalçın and many others for their friendship throughout the years in high school and university. Finally, I would like to express my gratitude to my family who has supported me in every decision I have taken and help me to be the person now.

High-performance dielectric substrate development with low D_k and D_f for RF and mm-wave applications

Umut Barış Gögebakan

EE, Master's Thesis, 2021

Thesis Advisor: Prof. Dr. Yaşar Gürbüç

Thesis Co-Advisor: Assoc. Prof. Güllü Kızıldaş Şendur

Keywords: Laminate Substrates, Dielectric prediction, mm-wave, Resin, Reinforcements, Electromagnetic and Mechanical modelling.

Abstract

For almost five decades, the industries were attracted towards silica-filled epoxy laminates due to their enhanced mechanical and electrical properties. Predominantly vast majority of the integrated circuits were packed by silica blended epoxy structures due to the ease of processability and cost reduction. However, in 5G applications, the signal that operates in the RF and mm-wave regions gets attenuated as it propagates along the PCB substrate made of epoxy-silica-based laminates. Hence, the need for low-loss laminates evolved to reduce the attenuation of the signal.

The effective dielectric properties need to be enhanced to develop a low-loss laminate. The effective dielectric properties of the PCB laminate are strongly dependent on their building blocks. Thus, due to the heterogeneous nature of the PCB laminates, the effective dielectric properties can be manipulated by the selection of host matrix, reinforcement type, or interfacial functionalization between these building blocks. The main parameters that affect dielectric materials are the dielectric constant (D_k) and the dissipation factor (D_f) which is described by the ratio between the imaginary part and the real part of the complex permittivity. EM wave transition from free space to a medium of a higher relative permittivity (ϵ_r), resulting in a slower velocity, shorter wavelength, and the amplitude will be reduced. More specifically, PCB laminate design efforts are primarily based on minimizing the real part of the permittivity (ϵ') to reduce the capacitive coupling and minimize the imaginary part of the permittivity (ϵ'') to reduce electrical loss.

The primary objective of this study is the modelling and the development of a high-performance, low-cost PCB substrate that operates in RF and mm-wave applications. In order to achieve these specifications, we have examined the particular building blocks of the PCB laminates and determined the targeted chemical structures of the host matrix and the specific fiber weave structures.

However, due to the lack of prediction techniques of the effective electrical and mechanical properties of the laminates, we have utilized multiple approaches to determine the effective electrical and mechanical properties of the laminate structures. In terms of effective electrical parameters, this thesis proposes two approaches: internal-field and energy-based approaches. Thus, both proposed methods consider the concept of the representative unit cell, which provides three-dimensional control over the unit volume of a laminate. Using single and two-level homogenization techniques, obtained local dielectric properties were converted into an effective dielectric property. With respect to the single level, the two-level homogenization technique creates an opportunity to extract effective dielectric properties of multi-layered laminates with a less computational load. Subsequently, both internal-field and energy-based approaches were verified with common effective medium approximations and compared with the measurement results between 20 GHz to 40 GHz. As a result in terms of the complex permittivity, the internal field approach predicted the effective D_k with a 2.5% error rate and the effective D_f predicted with 18.5% error rate with respect to the measurement results at 40 GHz.

On the other hand, to extract the effective mechanical properties, a two scale homogenization technique was proposed to examine the yarn behaviour of the laminate. These are yarn and laminate homogenization techniques. Thus, the simulation results of yarn homogenization were obtained to be inserted into the laminate homogenization scale.

RF ve mm-dalgaboyu Uygulamaları için Yüksek-Performanslı, Düşük D_k ve D_f Değerli Dielektrik Taban Malzemesi Geliştirimi

Umut Barış Göğebakan

EE, Yüksek Lisans Tezi, 2021

Tez Danışmanı: Prof. Dr. Yaşar Gürbüz
Tez Yardımcı Danışmanı: Doç. Dr. Güllü Kızıldaş Şendur

Anahtar Kelimeler: Laminat taban, Dielektrik kestirim, mm-dalgaboyu, Reçine, Güçlendirme Malzemesi, Elektromanyetik ve Mekanik Modelleme.

Özet

Neredeyse elli yıldır endüstriler, gelişmiş mekanik ve elektriksel özelliklerinden dolayı silika dolgulu epoksi laminatlara ilgi duymuştur. Ağırıklı olarak entegre devrelerin büyük çoğunluğu, işlenebilirlik kolaylığı ve maliyet düşüklüğü nedeniyle silika karışımli epoksi yapılar ile paketlenmiştir. Ancak 5G uygulamalarında RF ve mm dalga bölgelerinde çalışan sinyal, epoksi-silika bazlı laminatlardan yapılmış PCB substratı boyunca yayılırken zayıflar. Bu nedenle, sinyalin zayıflamasını azaltmak için düşük kayıplı laminatlara duyulan ihtiyaç gelişmiştir.

Düşük kayıplı bir laminat geliştirmek için etkili dielektrik özelliklerin geliştirilmesi gerekir. PCB laminatın etkin dielektrik özellikleri, laminatın yapı taşlarına büyük ölçüde bağlıdır. Bu nedenle, PCB laminatlarının heterojen doğası nedeniyle, etkin dielektrik özellikler, ana matris, takviye tipi veya bu yapı taşları arasındaki arayüz işlevselleştirme seçimi ile manipüle edilebilir. Dielektrik malzemeleri etkileyen ana parametreler, dielektrik sabiti ve karmaşık geçirgenliğin sanal kısmı ile gerçek kısmı arasındaki oran ile tanımlanan kayıp faktörüdür. Serbest uzaydan daha yüksek görelî geçirgenliğe sahip bir ortama EM dalga geçişi, daha yavaş bir hız, daha kısa dalga boyu ile sonuçlanır ve genlik azalır. Daha spesifik olarak, PCB laminat tasarım çabaları, öncelikle kapasitif kuplajı azaltmak için geçirgenliğin gerçek kısmını en aza indirmeye ve elektrik kaybını azaltmak için geçirgenliğin hayali bölümünü en aza indirmeye dayanmaktadır.

Bu çalışmanın temel amacı, RF ve mm dalga uygulamalarında çalışan yüksek performanslı, düşük maliyetli bir PCB alt tabakasının modellenmesi ve geliştirilmesidir. Bu spesifikasyonları elde etmek için, PCB laminatlarının belirli yapı taşlarını inceledik ve ana matrisin hedeflenen kimyasal yapılarını ve spesifik fiber örgü yapılarını belirledik.

Ancak, laminatların etkin ve mekanik özelliklerine ilişkin tahmin tekniklerinin yeterli olmaması nedeniyle, yapıların etkin elektriksel ve mekanik özelliklerini belirlemek için birden fazla yaklaşım kullandık. Etkin elektrik parametreleri açısından, bu tez iki yaklaşım önermektedir: iç alan ve enerji tabanlı yaklaşımlar. Bu nedenle, önerilen her iki yöntem de, bir laminatın birim hacmi üzerinde üç boyutlu kontrol sağlayan temsili birim hücre kavramını dikkate alır. Tek ve iki seviyeli homojenleştirme teknikleri kullanılarak, elde edilen yerel dielektrik özellikleri, etkin bir dielektrik özelliğe dönüştürülmüştür. Tek seviyeye göre, iki seviyeli homojenleştirme tekniği, daha az hesaplama yükü ile çok katmanlı laminatların etkin dielektrik özelliklerini çıkarmak için bir fırsat yaratır. Daha sonra, hem iç alan hem de enerji tabanlı yaklaşımlar, popüler etkin ortam yaklaşımlarıyla doğrulandı ve 20 GHz ile 40 GHz arasındaki ölçüm sonuçlarıyla karşılaştırıldı. Sonuç olarak, karmaşık geçirgenlik açısından iç alan yaklaşımı kullanılarak, 40 GHz'deki ölçüm sonuçlarına göre etkin D_k 'ı %2.5 hata oranıyla ve efektif D_f 'ı %18.5 hata oranıyla tahmin etmiştir.

Öte yandan, etkili mekanik özellikleri çıkarmak için laminatın iplik davranışını incelemek için iki ölçekli homojenizasyon tekniği önerildi. Bunlar iplik ve laminat homojenizasyon teknikleridir. Böylece, iplik homojenizasyonunun simülasyon sonuçları, laminat homojenizasyon ölçeğine eklenmek üzere elde edilmiştir.

Contents

Acknowledgements	v
Abstract	vi
List of Figures	xiv
List of Tables	xv
List of Abbreviations	xvi
1 Introduction	1
1.1 Motivation	3
1.2 Designing Laminates for Low D_k and D_f	5
1.3 Methodology	6
1.4 Organization	7
2 Background	8
2.1 Maxwell's Equations	8
2.2 Polarization	10
2.2.1 Electronic Polarization (P_e)	10
2.2.2 Atomic (Ionic) Polarization (P_a)	12
2.2.3 Orientational (Dipolar) Polarization (P_o)	13
2.2.4 Total Polarization	14
2.3 Complex Permittivity	15
2.3.1 Frequency Dependency of D_k and D_f	15
2.3.2 Temperature Dependency	17
2.4 Potential Materials Used in PCB Industry	20
2.4.1 Reinforcement Compositions	20
2.4.2 Host Matrix Selection	21

2.4.3	Potential Compositions	24
2.4.4	Relationship Between Dielectric Properties and GtRR	25
3	Modelling	26
3.1	Electromagnetic Modelling	26
3.1.1	Effective Complex Permittivity	26
3.1.2	Effective Medium Approximations	31
3.1.3	Simulation Setup and Results	33
3.2	Mechanical Modeling	44
3.2.1	Yarn Homogenization	44
4	Characterization	48
4.1	Fabry Perot Open Resonator(FPOR) Measurement	48
4.1.1	FPOR Measurements of the Functionalized Reinforced Composites	53
4.2	Split Post Dielectric Resonator(SPDR) Measurement	54
4.3	Design of a Ring Resonator Measurement Setup	56
5	Conclusion & Future Work	59
5.1	Summary of Work	59
5.2	Future Work	60
	APPENDIX	68
	References	71

List of Figures

2.1	Simple dipole moment	10
2.2	The origin of electronic polarization. a.) No electric field applied, $E = 0$ state, b.) Under an applied electric field Induced dipole moment of an atom	11
2.3	a.) Without E-Field, net dipole moment per ion zero, b.) Under the E-Field, ions will be displaced which leads net dipole moment per ion	13
2.4	a.) The induced dipole moment p decrease or relax from $\alpha_d(0) E_0$ to $\alpha_d(0)E$, b.) Sudden alteration of applied DC field from E_0 to E . . .	16
2.5	Frequency vs. ϵ_r' and ϵ_r'' curve for a generic dielectric materials	17
2.6	The temperature dependency of real part of the complex permittivity for the PPO based host matrix at 500 MHz	19
2.7	The temperature dependency of imaginary part of the complex permittivity for the PPO based host matrix at 500 MHz	19
3.1	Simple homogenization procedure of bi-phased composite structure: ϵ_i denotes the circular inclusions of the 2D host matrix, ϵ_h describes the permittivity of the host matrix, and ϵ_{eff} denotes the macroscopic permittivity response of the heterogeneous medium.	31
3.2	Determined simulation setup and boundary conditions for single level homogenization at 20 GHz	34
3.3	Illustration of the generic E-Glass fiber fabric's denotations of the dimensions	35
3.4	a.)Optical microscopy images of a.)106 type of E-Glass fiber fabric. b.)1080 type of E-Glass fiber fabric.	36
3.5	Illustration of the representative unit cell dimensions with respect to the introduced wavelength into the system. Generic representative unit element sizing till, a.)20 GHz, b.)50 GHz, c.)100 GHz	37
3.6	Simulation setup of the plane weave representation, a.)Total E-field distribution, b.)Local E-field distribution, c.)Assigned mesh at 800 MHz	38
3.7	Simulation setup of the bundle weave representation, a.)Total E-field distribution, b.)Local E-field distribution, c.)Assigned mesh at 20 GHz	38

3.8	Single level homogenization procedure with the bundle weave representation. a.)Determined fiber bundles for 106 type E-Glass fabric. b.)Total geometry of the simulation setup and homogenized region at 40 GHz.	39
3.9	Two level homogenization procedure with the bundle weave representation. a.)Determined fiber bundles for warp direction 1080 type E-Glass with host matrix. b.)Determined fiber bundles for weft direction 1080 type E-Glass with host matrix. c.)Second level homogenization	40
3.10	Simulation results of effective dielectric constant, via internal field and energy based approaches under single level homogenization procedure compared with common effective medium approximations for E-Glass(106)+PPO composition.	41
3.11	Simulation results of effective dissipation factor, via internal field and energy based approaches under single level homogenization procedure compared with common effective medium approximations for E-Glass(106)+PPO composition.	41
3.12	Simulation results of effective dielectric constant, via internal field and energy based approaches under single and two level homogenization procedures compared with common effective medium approximations for E-Glass(1080)+PPO composition.	42
3.13	Simulation results of effective dissipation factor, via internal field and energy based approaches under single and two level homogenization procedures compared with common effective medium approximations for E-Glass(1080)+PPO composition.	42
3.14	Developed model to extract the effective mechanical properties of the unit cell	45
4.1	Cross-sectional illustration of the Fabry Perot Open Resonator. . . .	49
4.2	The realized measurement setup between 20 GHz to 40 GHz for FPOR measurements.	49
4.3	E-Glass(106) reinforced PPO based composite's single level homogenization based modelling compared with the measurement results of dielectric constant via FPOR between 20 GHz to 40 GHz	50
4.4	E-Glass(106) reinforced PPO based composite's single level homogenization based modelling compared with the measurement results of dissipation factor via FPOR between 20 GHz to 40 GHz	51

4.5	E-Glass(1080) reinforced PPO based composite's both single and two level homogenization based modelling compared with the measurement results of dielectric constant via FPOR between 20 GHz to 40 GHz	52
4.6	E-Glass(1080) reinforced PPO based composite's single and two level homogenization based modelling compared with the measurement results of dielectric constant via FPOR between 20 GHz to 40 GHz . . .	52
4.7	Cross-sectional illustration of the Split Post Dielectric Resonator. . .	54
4.8	The realized measurement setup at 10 GHz for SPDR measurements.	55
4.9	The layout of the designed micro-strip ring resonator in ADS on a arbitrarily defined substrate at 10 GHz	56
4.10	Extracted scattering parameters of the ring resonator from the ADS simulations	57
4.11	Designed micro-strip ring resonator simulation setup in COMSOL at 10 GHz	57
4.12	Extracted scattering parameters of the ring resonator from the COMSOL multi-physics simulations	58
5.1	The effective dielectric properties measurements of the functionalized reinforcements as function of frequency. a.) Experiment set with functionalized E-Glass(106)+PPO, b.) Experiment set with functionalized E-Glass(1080)+PPO	66
5.2	Cross-sectional SEM image of an untreated 1080 type E-Glass with PPO based composite.	67
5.3	Cross-sectional SEM image of an vinylsilane (VTES) treated 1080 type E-Glass with PPO based composite.	67

List of Tables

1.1	Proposed material specifications	3
1.2	Properties of common host matrix materials for PCB substrates. . .	4
2.1	Material properties of the PPO based host matrix	18
2.2	D_k and D_f values of certain reinforcement materials	20
2.3	Compositions of particular reinforcements	21
2.4	D_k and D_f values of certain resin systems	21
2.5	Desirable and undesirable groups for resin matrix	23
2.6	Compositions of particular reinforcements	25
3.1	Dimensions of reinforcement as a E-Glass fiber fabric	36
3.2	Comparison of cell periodicity yarn homogenization with mixture rules results	46
4.1	SPDR measurements of 106 and 1080 type reinforced PPO based composites at 10 GHz	54
5.1	SPDR measurements of 106 and 1080 type functionalized reinforced PPO based composites at 10 GHz	65

List of Abbreviations

APTES	(3-Aminopropyl)triethoxysilane
BIE	Boundary Integral Equations
CMR	Classical Mixing Rules
CTE	Coefficient of Thermal Expansion
D_f	Dissipation Factor
D_k	Dielectric Constant
E-Glass:	Electronic Grade Glass
EM	Electromagnetic
EMA	Effective Medium Approximation
FDM	Finite Difference Method
FDTD	Finite Difference Time Domain
FEM	Finite Element Method
FDMA	Frequency Division Multiple Access
FDD	Frequency Division Duplexing
FPOR	Fabry Perot Open Resonator
FR-4	Flame Retardant 4 (Printed Circuit Board)
GPTES	(3-Glycidyloxypropyl)trimethoxysilane
GTRR	Glass To Resin Ratio
IC	Integrated Circuit
IL	Insertion Loss
LOO	Looyenga Approximation
LTCC	Low Temperature Co-fired Ceramics
MG	Maxwell Garnett Approximation
mm-Wave	millimeter Wave
MUT	Material Under Test
PBC	Periodic Boundary Conditions
PCB	Printed Circuit Board
PPO	P-Phenylene Oxide
PTFE	Polytetrafluoroethylene
RF	Radio Frequency
RVE	Representative Volume Element
SB	Symmetric Bruggeman Approximation
SEM	Scanning Electron Microscopy
SMA	Sub Miniature version A
SPDR	Split Post Dielectric Resonator
VTES	Vinyltriethoxysilane

1 Introduction

The history of modern PCB technology, which utilizes SMD, can be traced back to the early 1960s. The PCB technology used copper cladding insulating material as their printed board laminate. Since the frequency of the EM wave propagating in the PCB board was less than MHz range, the dielectric properties of the printed board laminate were not of importance. With the advancement of communication technologies, the RF or mm-wave regions paved way to the enhancement of the current technology. However, in these regions, the EM waves get attenuated due to the lossy dielectric properties of the laminate. Therefore, there became a need to develop improved laminate materials with low loss dielectric properties.

The interest of the market, for the low dielectric constant (D_k) and low dissipation factor (D_f) have been evolving to grow as wireless communications have become more available to the consumers. Furthermore, the transition of an EM wave from the free space to a medium, which has a higher relative permittivity, results in a reduction of velocity and wavelength and attenuation of the wave. Due to this, the performance parameter of the circuit is affected by the dielectric constant of the substrate such as the propagation constant of the signal and the size of the board. On the other hand, the D_f of the PCB laminates determines the dielectric losses. Thus, it will determine the integrity of the signal across the transmission lines. Moreover, the loss mechanism is mainly driven by the resistance of the conductors and the attenuation of the EM wave in the substrate [1–3]. As a result, the dielectric losses of the material will produce a power loss in the signal due to the translation of absorbed signal power to the heat emission. The power loss of the propagating signal can be reduced by using a material with a low loss property; this will result in a lesser power absorption from the signal. This becomes advantageous in the receiver side of a communication system because the low loss substrate material, increases the antenna sensitivity and hence, a clear signal is received by the antenna. Moreover, when the power dissipated by the signal is reduced, the battery lifetime is increased [1].

Due to the heterogeneous nature of the PCB laminates, the building materials (host matrix and reinforcement) of the laminates carry vital importance in determining the effective electrical and mechanical properties. Therefore, the primary objective of this study is the modelling and the development of a high-performance, low-cost PCB substrate that operates in RF and mm-wave applications. Thereby, we examined and proposed the potential building block's materials of the PCB laminates and found that selecting the PPO-based host matrix and the particular

E-Glass compositions can be a viable solution for the application interest. In order to determine the proposed composition's effective dielectric properties and the manufactured substrates, this thesis proposes the energy-based and internal field approaches via single and two-level homogenization techniques by using commercially available COMSOL Multiphysics software. Hence, the techniques mentioned were evaluated by the effective medium approximations and compared with measurement results between 10 GHz and 40 GHz. Therefore, the measurements conducted via Fabry Perot Open Resonator (FPOR) and Split Post Dielectric Resonator (SPDR) to evaluate the copper cladding performance of the modelled composite structures we have proposed Ring Resonator structure to compare with the bare laminate measurement results. Subsequently, the Yarn homogenization method was utilized and verified with the mixture rules to determine the effective mechanical properties of the proposed laminates. Consequently, to enhance the proposed substrate's dissipation factor, the proposed E-Glass types functionalized and measurement results are presented in Appendix E.

1.1 Motivation

This study proposes to develop a design methodology for polymer core substrate with low dielectric constant, low loss, high thermal conductance, and low coefficient of thermal expansion (CTE). The proposed substrate should have the ability to operate at 94 GHz for mm-wave antenna applications. The potential dielectric constant of a microstrip antenna substrate is in the range of 2.2 to 12. In order to obtain larger bandwidth, higher efficiency, and loosely bound fields in an antenna, the desirable dielectric constant of the thick substrate should be located at the low end of the mentioned range [1]. In order to reduce the electrical loss during transmission, the low dissipation factor is required. On the other hand, low CTE provides thermal stability in multilayered laminates with respect to the thermal variations, and, finally, high thermal conductance is required to exhibit heat dissipation on the laminate structure. Thus, in Table 1.1, proposed material specifications are presented.

Table 1.1: Proposed material specifications

Properties	Target Value
Permittivity (D_k)	3
Loss tangent (D_f)	0.006 (40 GHz)
Coefficient of Thermal Expansion (α)	$10^{-5}(1/C)$
Thermal Conductance (k)	30 (W/mC)

As mentioned above, provided specifications are a viable option for high-frequency antenna application. Therefore, to proceed with a design procedure of newly developed laminate structures because of such specifications, the selection of the host matrix is made by examining the available products on the market. The general properties of common host matrix materials for PCB applications are presented in Table 1.2. According to the provided permittivity range for antenna applications, the Ceramics and Plastic-Ceramic compositions are directly eliminated due to the higher permittivity nature. Therefore, the Low-K polymers can be a potential host matrix to utilize in high-frequency antenna substrates. According to the extracted data from the commercially available resin products presented in further sections, the PPO-based host matrix is selected due to the low permittivity and low loss of nature. As mentioned in the further sections, the E-Glass type reinforcement is selected due to its low loss and high availability.

However, the design procedure of new composite material and the electrical properties prediction through the effective parameters is also essential. The design methodology of this study depending on FEM simulations and characterization of

Table 1.2: Properties of common host matrix materials for PCB substrates.

Properties [4]	D_k	$\tan(\delta)$	CTE	Metal Adhesion
Low-K polymers	2 - 5	0.0001 - 0.01	Poor	Poor - Good
Plastic/Ceramic Comp.	3 - 50	0.0001 - 0.01	Good	Poor - Good
Glasses	3 - 12	0.00005 - 0.005	Good	Good
Ceramics	10 - 500	0.00005 - 0.005	Good	Good

the fabricated PCB laminates. The designer would have gained control over the component geometry, volume ratio, and the distribution types of the composite structures [5]. Predicting a composite's electrical properties, in this case, a mixture that contains different materials has been quite a challenging task. It carries vital importance from both theoretical and practical points of view [6], [7]. Instead of the trial and error method, achieving high accuracy on the composite structures' electrical properties requires several simulations and numerical validations. To such a degree, the determination of the dielectric properties of the multi-phase composite systems gains attention from the packaging and PCB industries for several years.

1.2 Designing Laminates for Low D_k and D_f

In order to obtain a low D_f in a laminate system, three factors should be carefully considered to design a new resin system with low dielectric properties. These factors:

- Impurities
- Moisture absorption characteristics
- Structure of the polymer

In terms of impurities, ionic contamination is one of the impurity mechanisms in a resin system. Such catalysts in the resin system can increase the conductivity of the laminate structure, which results in alteration in D_k and D_f values [3, 4]. Subsequently, moisture absorption characteristics influence the dielectric properties of the material by increasing the polarity of the host matrix of the PCB; as the polarity alteration increases in the resin system, the D_k and D_f will be altered. Finally, the polymer structure influences the dielectric constant of the synthesized material, especially for low D_k and D_f values; the material should have highly symmetric and contain a smaller number of polar groups. To control the dielectric properties of potential material, the reactive end group, polar structural moieties, and curing mechanisms can be optimized with respect to the desired specifications [3].

Consequently, as mentioned, both resin and reinforcement contribute to the substrate's electrical performance. In the literature, most conventional methods for controlling the D_k and D_f of a PCB laminate are mainly based on chemical manipulation of resin's polymer structure [3, 8]. However, more recently, there is a growing interest in developing low dielectric reinforcement solutions for manipulating the D_k and D_f by using enhanced glass fiber fabrics such as S-Glass and D-lass type of reinforcements. These solutions are comprehensively discussed in the further sections.

1.3 Methodology

Several formulations derive the dielectric constant of the bi-phased composites such as Maxwell-Garnett effective medium approximation. These formulations are based on the well known dielectric mixture rules as a function of fiber volume ratio; however, most of the formulations are limited with a calculation of a single value or determination of the higher and lower limits of the bi-phased composites; therefore, the anisotropy on the laminate may not be clearly represented.

The effective permittivity of a multi-phased structure can be defined as an average property. That links the composite structure's internal morphology (dielectric and shape characteristics, spatial arrangement of inclusions, volume fraction) with the bulk sample's dielectric property [5]. This concept has been introduced using the finite element method (FEM), with a series of articles by Tuncer et al. [6, 9–11]. These article series introduced the representative volume element (RVE), a concept for simulating ordered and disordered binary composites. The RVE concept is based on the definition of a minimum periodic unit cell. This unit cell concept includes the smallest periodic structure where the fillers and the geometrical structures are located in the unit cell [5].

In order to determine the effective dielectric properties and wideband frequency behavior of the composites, the definition of a unit cell is one of the critical aspects of modelling the periodic structures. Thus, the determination of the unit cell creates an ability to utilize the proposed effective medium approaches to extract the effective dielectric properties into the macroscopic scale by utilizing internal field and energy-based approaches. Finally, these effective medium approaches have been compared with the effective medium approximations such as Maxwell-Garnett, Symmetric Bruggeman, and Looyenga approximations. Additionally, direct modeling of fiber weave structures inside a resin matrix would require an enormous amount of computational resources, and it would violate minimum entity dimensions of the structure in particular frequencies. Therefore, we have utilized the homogenization procedure by using periodic boundary conditions in our representative unit cell. Furthermore, process-related uncertainties can be introduced into the modeling environment, such as uniform air defects and the expansion of the fiber weaves.

1.4 Organization

The organization of the following chapters is arranged as follows: Chapter 2 provides the fundamentals of the Maxwell's equations employed during the simulations. To characterize the PCB materials the three polarization mechanisms (Orientational (dipolar), Atomic (Ionic), and Electronic) and complex permittivity are scrutinized. Different types of the potential materials that can be used in PCB development are briefly explained.

Chapter 3 contains the modeling part of the heterogeneous composites of the PCB. Firstly, the electromagnetic modeling of the proposed compositions is considered. The different models used to determine the effective dielectric properties are introduced. Subsequently, the simulation setup, boundary conditions, and effective medium approximations will be evaluated. Finally, the mechanical modeling of the representative unit-cell is presented through the evaluation of the yarn and laminate homogenization.

Chapter 4 demonstrates the characterization of fabricated composites in terms of their dielectric properties through different methods for various values of frequencies. The effective dielectric properties have been measured employing different techniques such the Fabry Perot Open Resonator (FPOR), Split Post Dielectric Resonator (SPDR). Additionally, the design and potential measurement technique proposed. The results of the FPOR technique and the ones of the modeling are compared for the range of frequencies from 20 GHz to 40 GHz. Using SPDR technique results of the effective dielectric constant and dissipation factor are extracted more precisely. In section 4.4 the extraction method, design, and simulation of the above mentioned extracted parameters is delineated.

Chapter 5 provides a brief summary about the study and opens up a discussion about the evaluation of the simulations and measurements. Subsequently, future work finalizes the thesis.

2 Background

2.1 Maxwell's Equations

The four fundamental equations governing electromagnetic waves are Gauss's law, Faraday's Law, Gauss's law for magnetism and, Maxwell-Ampere's law as presented in equations (2.1.1), (2.1.2), (2.1.3) and, (2.1.4) [12, 13].

$$\nabla \cdot \mathbf{D} = \rho_v \quad (2.1.1)$$

$$\nabla \times \mathbf{E} = -\frac{\partial \mathbf{B}}{\partial t} \quad (2.1.2)$$

$$\nabla \cdot \mathbf{B} = 0 \quad (2.1.3)$$

$$\nabla \times \mathbf{H} = \mathbf{J} + \frac{\partial \mathbf{D}}{\partial t} \quad (2.1.4)$$

where, \mathbf{D} denotes for the electric displacement field, ρ_v denotes for the charge density in a unit volume, \mathbf{E} denotes for the electric field, \mathbf{B} denotes for the magnetic flux density, \mathbf{H} denotes for magnetic field and, \mathbf{J} describes the current density. These Maxwell's equations are also considered as macroscopic level equations and are commonly called as the Maxwell's equations in matter. Maxwell's equation for time-harmonic fields can be written in the phasor form by the insertion of $e^{j\omega t}$. The time harmonic version of the Maxwell's equation can be described as in equations (2.1.5), (2.1.6), (2.1.7) and, (2.1.8) [12, 13].

$$\nabla \cdot \mathbf{D} = \rho_v \quad (2.1.5)$$

$$\nabla \times \mathbf{E} = -j\omega \mathbf{B} \quad (2.1.6)$$

$$\nabla \cdot \mathbf{B} = 0 \quad (2.1.7)$$

$$\nabla \times \mathbf{H} = \mathbf{J} + j\omega\mathbf{D} \quad (2.1.8)$$

Maxwell's equation for time-harmonic fields are common used because vast majority of the excitations in simulation environments are sinusoidal. The ability of solving with the time dependence can be realized by multiplying with the complex exponential term [14]. Therefore, by utilizing Maxwell-Ampere's and Faraday's laws, the flux of power will be described through the Poynting theorem, and the energy-based approach will be determined to extract effective dielectric properties in terms of the mean density of electric energy. Subsequently, the field vectors in a medium are described by the constitutive relations presented as in equations (2.1.9), (2.1.10) and (2.1.11). Hence, constitutive relations will be utilized in the internal field approach to extract the effective dielectric properties of a heterogeneous medium by surface/volume averaging. Further derivations of both the internal-field and energy-based approaches will be presented in Chapter 3.

$$\mathbf{D} = \varepsilon_0\mathbf{E} + \mathbf{P} \quad (2.1.9)$$

$$\mathbf{B} = \mu\mathbf{H} \quad (2.1.10)$$

$$\mathbf{J} = \sigma\mathbf{E} \quad (2.1.11)$$

where, \mathbf{P} denotes the polarization, μ denotes the permeability and σ denotes the conductivity of the medium.

2.2 Polarization

When an electric field is applied on a dielectric material, the bound charges get separated and induces an electric dipole moment. The electric displacement field vectors is represented as previously mentioned equation (2.1.9).

$$\mathbf{D} = \epsilon_0 \mathbf{E} + \mathbf{P} \quad (2.2.1)$$

where \mathbf{P} denotes the polarization which is induced by the related dipole moments. There are multiple polarization mechanisms in a dielectric material: these are Electronic polarization (P_e), Atomic (Ionic) polarization (P_a), Orientational (Dipolar) polarization (P_o), and Space – Charge polarization. Based on the dielectric theory, the electric dipole moment is an essential concept for measuring electrostatic effects in the dielectric medium [15].

Dielectric materials that are used in the PCB industry for couple of decades commonly called as the "linear dielectric" which corresponds to the induced polarization is dependent to the E-field. These materials utilized in the PCB industry are used in high-frequency applications [16]. Such that a generic ideal dielectric material does not involve polarizable bonds and delocalized electrons. [3]

2.2.1 Electronic Polarization (P_e)

The essence of electronic polarization lies on the segregation among the positive and the negative charges as shown in Figure 2.1 called dipole moment and denotes as \mathbf{p} . Therefore, electrical dipole moment has presented as in Equation (2.2.2), where Q denotes for the charges that are equal each other in magnitude and \mathbf{a} denotes the vector from negative charge to positive charge [15].

$$\mathbf{p} = Q\mathbf{a} \quad (2.2.2)$$

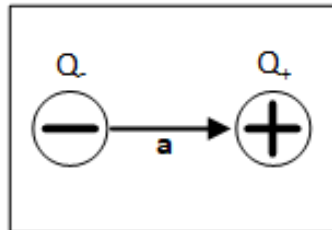


Figure 2.1: Simple dipole moment

Induced dipole moment emerges due to the applied electric field. Therefore, to extract the induced dipole moment “ $p_{induced}$ ” by utilizing the equation (2.2.3) as presented below.

$$\mathbf{P}_{induced} = \alpha_e \mathbf{E} \quad (2.2.3)$$

where, (α_e) denotes the electronic polarization coefficient also defined as the polarizability of the atom. In order to find the material property of the electronic polarizability of α_e can be extracted by the equation (2.2.4) [15].

$$\alpha_e = \frac{Ze^2}{m_e \omega_0^2} \quad (2.2.4)$$

where, the “Z” stands for the number of electrons orbiting the nucleus, m_e denotes the mass of electron, and ω_0 describes the resonance frequency of the electronic polarization mechanism. As it stated in equation (2.2.3) the induced dipole moment emerges from the applied electric field as shown in Figure 2.2. The distributions of positive and negative charges have segregated as shown Figure 2.2b [15].

On examining the electronic polarizability guides us to extract the electrical properties of the materials. To discover the macroscopic electrical properties of the materials by utilizing the microscopic electrical properties, the determination of the vector of polarization create a guidance to extract the relative permittivity of the material. The vector of polarization denotes as \mathbf{P} is simply the multiplication of the total number of molecules in the selected volume element which denotes as N with a mean dipole moment per molecule p_{av} . Therefore, Kasap et al. determines

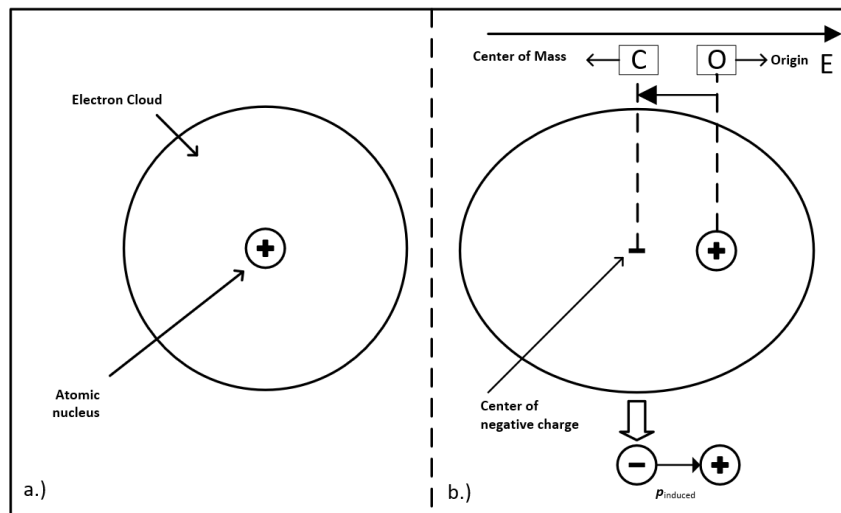


Figure 2.2: The origin of electronic polarization. a.) No electric field applied, $E = 0$ state, b.) Under an applied electric field Induced dipole moment of an atom

the dependence of the polarization vector which denotes as \mathbf{P} under an applied electric field of \mathbf{E} with the electrical susceptibility, χ_e . Thus, the polarization vector determined as $\mathbf{P} = \chi_e \varepsilon_0 \mathbf{E}$. Consequently, the relative permittivity of a medium in terms of polarizability is shown in equation (2.2.5) [15].

$$\varepsilon_r = 1 + \frac{N\alpha_e}{\varepsilon_0} \quad (2.2.5)$$

As mentioned in the further sections the Electronic polarization is the main polarization mechanism at range of 10^{16} Hz range, which extremely exceeds the relevant frequency range of this study.

2.2.2 Atomic (Ionic) Polarization (\mathbf{P}_a)

Ionic polarization emerges in ionic crystals and they have distinctly located at precise lattice structures such that KCl and NaCl. The oppositely charged adjacent pair of ions create a dipole moment among each other. As shown in the Figure 2.3a, the net polarization among the crystal structure will be equal to the zero because of the dipole moments in opposite directions will balance each other, under the zero electric field conditions. This phenomenon indicated as in equation (2.2.6) [15].

$$p_{net} = p_+ - p_- \quad (2.2.6)$$

However, as in stated in figure 2.3b under an applied electric field, the net dipole moment will no longer be zero. Thus, the induced average dipole moment among the ion pairs ($p_{average}$) have dependency on the electric field, therefore, atomic (ionic) polarizability (α_i) defined as in (2.2.7).

$$p_{average} = \alpha_i \mathbf{E}_{Local} \quad (2.2.7)$$

To extract the macroscopic electrical properties from the microscopic electrical properties, Clausius-Mossotti equation will be utilized. Therefore, relative permittivity (ε_r) determined through the microscopic polarization phenomena by the dependency of the atomic (ionic) polarizability which denoted as α_i .

$$\frac{\varepsilon_r - 1}{\varepsilon_r + 2} = \frac{N\alpha}{3\varepsilon_0} \quad (2.2.8)$$

To obtain the relative permittivity (ϵ_r) in terms of the ionic (atomic) polarization in a solid media equation (2.2.9) will be utilized. Hence, the polarization which governs by the ionic (atomic) polarization mechanism described in terms of the local electric field distribution and relative permittivity of the solid media as shown in the equation (2.2.10) [15].

$$p_a = N_i p_{average} \quad (2.2.9)$$

$$p_a = (\epsilon_r - 1)\epsilon_0 \mathbf{E} \quad (2.2.10)$$

Thus, as it stated in equation (2.2.8) by utilizing the Clausius-Mossotti equation, atomic (ionic) polarizability could be expressed in terms of relative permittivity (ϵ_r) as shown in equation (2.2.11).

$$\frac{\epsilon_r - 1}{\epsilon_r + 2} = \frac{N_i \alpha_i}{3\epsilon_0} \quad (2.2.11)$$

2.2.3 Orientational (Dipolar) Polarization (\mathbf{P}_o)

In the concept of orientational (dipolar) polarization mechanism particular molecules acquires behaviour of the permanent dipole moments p_0 , such as HCl. The bonds among the H^+ and Cl^- are almost rigid and holds them in intact;

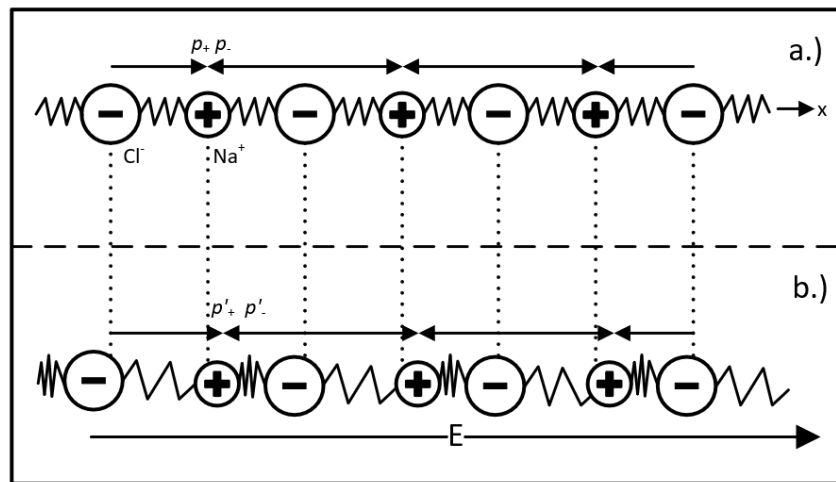


Figure 2.3: a.) Without E-Field, net dipole moment per ion zero, b.) Under the E-Field, ions will be displaced which leads net dipole moment per ion

therefore, these molecules in their center of mass, exposed to a torque (τ). Emerged torque creates a rotation on molecule which, adjusts the direction of the permanent dipole moment under the effect of electric field. Therefore, the polarization occurs through the permanent dipole moments described as in equation (2.2.12) [15].

$$P = Np_0 \quad (2.2.12)$$

where, "N" denotes the number of molecules per unit cell. In the steady state molecules presents random motion and collisions among them selves due to material thermal energy. Therefore, in steady state both random motion and the collisions eliminates the alignments of the dipole moments by preventing the dipole orientations. However, in the presence of the electric field orientational (dipolar) polarization dominates unit cell hence, mean dipole moment per unit molecule can be described as " $p_{average}$ ".

$$p_{average} = \frac{1p_0^2\mathbf{E}}{3kT} \quad (2.2.13)$$

where, p_0 denotes for permanent dipole moment, k denotes for Boltzmann constant, T denotes for temperature in Kelvin, and \mathbf{E} denotes for applied electric field. Furthermore, the division of " $p_{average}$ " to applied electric field ends up with the orientational (dipolar) polarizability " α_d " which presented in equation (2.2.14).

$$\alpha_d = \frac{1p_0^2}{3kT} \quad (2.2.14)$$

As a result, the orientational (dipolar) polarizability (" α_d ") decreases with the increasing temperature trend. Therefore, the relative permittivity (ϵ_r) also decreases with the increasing temperature in gas and liquid phases [15].

2.2.4 Total Polarization

The total polarization described as the summation of all three polarization mechanisms (Orientational (dipolar), Atomic (Ionic), and Electronic). Therefore, mean dipole moment for a particular molecule presented in equation (2.2.15).

$$p_{total} = \alpha_e\mathbf{E}_{Local} + \alpha_i\mathbf{E}_{Local} + \alpha_d\mathbf{E}_{Local} \quad (2.2.15)$$

In the presence of both electronic and atomic (ionic) polarization mechanisms, Clausius – Mossotti equation can be utilized to extract the relative permittivity of a medium which, presented in equation (2.2.16). However, orientational (dipolar)

polarization can not be described by the Clausius – Mossotti equation to extract relative permittivity in terms of polarizability.

$$\frac{\varepsilon_r - 1}{\varepsilon + 2} = \frac{N_i\alpha_i + N_e\alpha_e}{3\varepsilon_0} \quad (2.2.16)$$

2.3 Complex Permittivity

The complex permittivity of the material describes the dielectric behaviour of the material as a function angular frequency (ω) hence, the definition of the complex permittivity presented in equation (2.3.1) [17].

$$\varepsilon(\omega) = \varepsilon'(\omega) - j\varepsilon''(\omega) \quad (2.3.1)$$

There are multiple mechanisms that influence on the complex permittivity of the material over broad frequency range. As mentioned earlier these are electronic, atomic, orientational (dipolar) and, space - charge (interfacial) mechanisms, in this study most of the complex permittivity contribution introduced by the orientational (dipolar) polarization mechanism. Therefore, under an applied electric field, the macroscopic response of the dielectric material primarily governed by the dipolar polarization mechanism where, introduces a phase shift among the \mathbf{P} and \mathbf{E} . As a result, the introduced phase shift will also effect the displacement field due to the contribution of \mathbf{P} [18]. Both energy storage and dissipation are describing the medium and field interactions. Hence, the real part of the complex permittivity determines the rate of energy storage of material under an alternating or static electric field. On the other hand, the imaginary part of the complex permittivity determines the capability of the dissipation of energy in terms of heat, due to the applied electric field which is also corresponds to loss factor of the material [17,19].

2.3.1 Frequency Dependency of \mathbf{D}_k and \mathbf{D}_f

The response of polarization under the DC conditions described by the concept of static dielectric constant. Whereas, the excitation of a material by sinusoidal variations corresponds to dielectric constant under AC conditions which, differs from the static case in generic materials. The direction and the magnitude repeatedly alter, in the presence of the field with a sinusoidal variations. Hence, this continuous alterations, disrupts the alignment of the dipoles in a single directions, in each cycle

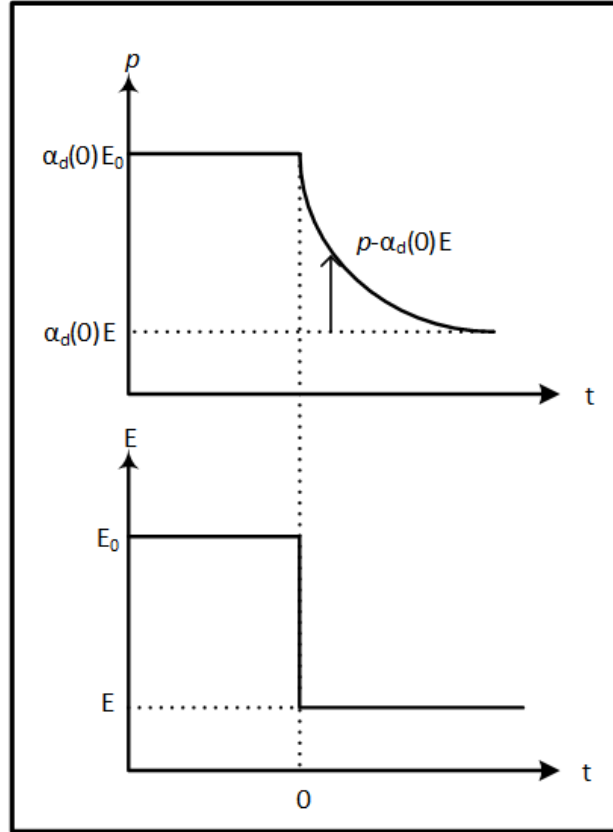


Figure 2.4: a.) The induced dipole moment p decrease or relax from $\alpha_d(0)E_0$ to $\alpha_d(0)E$, b.) Sudden alteration of applied DC field from E_0 to E

dipoles will try to align in a different direction however, dipoles, can not react to sinusoidal variations instantaneously in solid-state media. As a result, the immediate variations of the applied field can not be followed by the dipoles (as it shown in figure 2.4), substantially, rest of the dipoles randomly aligned among them. Hence, orientational (dipolar) polarizability (" α_d ") will become zero where, the ability of field will not be enough to induce a dipole moment at higher frequencies. As a result, induced dipole-moment can be extracted instantaneously through equations (2.2.13) and (2.2.14) [15].

In Figure 2.5, ϵ_r' and ϵ_r'' variation presented across the large frequency range. As seen in provided graph as the frequency increases, the relative permittivity of the generic material decreases. Therefore, from couple of hundreds kHz range to GHz range, the relative permittivity variation governed by the orientational (dipolar) polarization mechanism. Hence, the interaction between the varying electric field and the substrate material is depending on the rotation and the displacement of dipoles. By means, dipole displacement could be described as D_k or ϵ_r . Additionally, molecular friction and rotation of the dipoles described as the concept of $\tan(\delta)$. According to Kasap et al. the dispersion can be described as the rate of change of

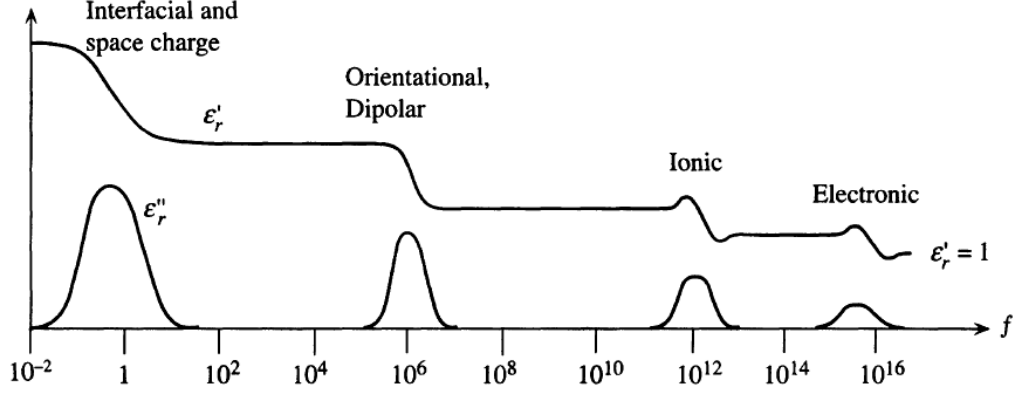


Figure 2.5: Frequency vs. ϵ'_r and ϵ''_r curve for a generic dielectric materials

the D_k across the range varying frequency band. As mentioned earlier, the dipole-moment relaxation contributes to dispersion at low frequencies therefore, has lower effect on the D_k dispersion at the interested frequency range [15].

2.3.2 Temperature Dependency

As mentioned earlier the temperature dependency of a material strongly contributed by orientational (dipolar) polarization mechanism thus, this dependency, introduced by the equation (2.2.14). According to Kasap et al. the relative permittivity, orientational (dipolar) polarizability, decreases as increasing temperature; as a result, the relative permittivity of the medium also decreases. However, this situation strongly valid for the polar liquids and gasses which involves permanent dipoles with in their structure. Whereas, this mechanism can also emerges on solids which, involves permanent dipoles in their chemical structure [15].

Due to the related frequency range of this study, the electrical properties of the proposed materials are primarily determined by the orientational (dipolar) polarization mechanism. When its consider that the dispersion of the dipolar dielectric material, can be described by the Debye equations. The Debye dispersion model is an ideal material model which is introduced by the P. Debye hence, it is based on both relative permittivity contributions and the relaxation time of the materials. Therefore, to find the complex relative permittivity by utilizing the Debye model is shown in equation (2.3.2) [20].

$$\epsilon_r = \epsilon_\infty + \frac{\epsilon_{dc} - \epsilon_\infty}{1 - j\omega\tau} \quad (2.3.2)$$

where, ϵ_{dc} denotes for the relative permittivity at dc conditions, ϵ_∞ denotes for the relative permittivity at high frequency, ω denotes for the angular frequency and, τ

Table 2.1: Material properties of the PPO based host matrix

Material Properties	Values
ϵ'_{dc}	2.617
ϵ'_{∞}	2.501
ϵ''_{dc}	0.00176
ϵ''_{∞}	0.0112
Relaxation Time (s)	1.40877E-10

denotes for the relaxation time. Hence, Debye dispersion model can be described as both the real and the imaginary part of the complex permittivity these are shown in equations (2.3.3) and (2.3.4).

$$\epsilon'_r = \epsilon_{\infty} + \frac{\epsilon_{dc} - \epsilon_{\infty}}{1 + (\omega\tau)^2} \quad (2.3.3)$$

$$\epsilon''_r = \frac{(\epsilon_{dc} - \epsilon_{\infty})(\omega\tau)}{1 + (\omega\tau)^2} \quad (2.3.4)$$

The relaxation time τ described from the Arrhenius equations which, is a function of temperature, shown in equation (2.3.5) [20].

$$\tau = \tau_0 \exp \frac{\zeta}{k_B T} \quad (2.3.5)$$

where, τ_0 denotes for the relaxation time constant, ζ denotes for the activation energy that is required for the dipole orientation, k_B denotes Boltzman constant and, T denotes for the temperature in Kelvin. To obtain the temperature dependency of the host matrix Debye dispersion model utilized. As a result, the temperature dependency of PPO based host matrix presented at 500 MHz for both real and imaginary parts of the complex permittivity presented as in both Figures 2.6 and 2.7. The proposed calculation was conducted in MATLAB, and the codes are presented in Appendix A and B. The corresponding materials properties to obtained the temperature dependency for different relaxation time constants were presented in Table 2.1.

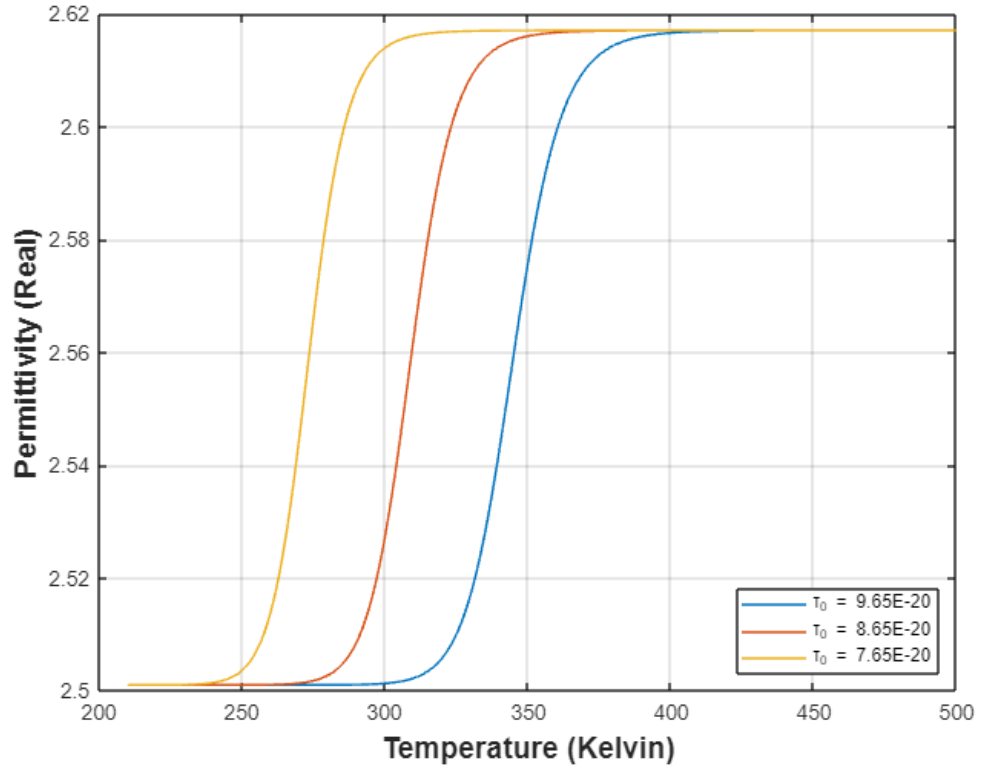


Figure 2.6: The temperature dependency of real part of the complex permittivity for the PPO based host matrix at 500 MHz

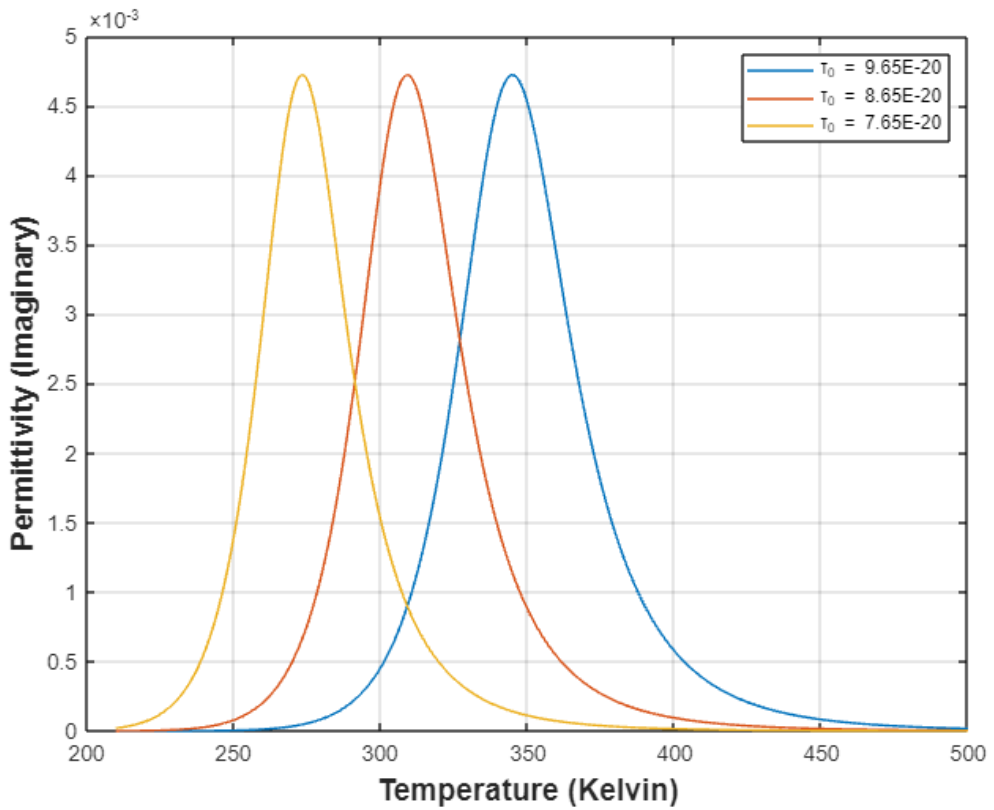


Figure 2.7: The temperature dependency of imaginary part of the complex permittivity for the PPO based host matrix at 500 MHz

2.4 Potential Materials Used in PCB Industry

2.4.1 Reinforcement Compositions

Materials used for manufacturing the PCBs are extensively composite material, typically including resin matrix, fibrous reinforcement, and copper foil. Electrical properties between reinforcement materials and resins are different from each other. One of the most widely used laminates in electronics is FR-4, which stands for flame retardant, made from epoxy resin and E-glass fabric [21]. Glass fibers are extensively used as reinforcement materials for polymer composite materials. Glass fiber reinforced polymer composites can be designed to accomplish specific electrical properties of the total substrate material. In addition to the electrical properties of the substrates, the mechanical properties of the substrate have importance to successful and low-cost manufacturing processes [8]. Therefore we have present the D_k and D_f values of certain reinforcement materials in Table 2.2.

Table 2.2: D_k and D_f values of certain reinforcement materials

Reinforcement [21]	D_k	D_f
E-Glass	6.3	0.0037
S-Glass	6	0.0020
D-Glass	4.6	0.0015
Quartz	4.6	0.0002

- **E-glass:** Inorganic E-glass as a reinforcement of laminates intended for high-speed digital applications, it has high D_k and low cost.
- **S-glass:** Inorganic S-glass is being investigated as a potential replacement for E-glass as reinforcement in laminates and composites for high-speed applications.
- **D-glass:** Inorganic D-glass was specifically developed as glass with improved dielectric properties for high-performance electronic applications. However, it involves some complications due to the high composition rate of SiO_2 .
- **Quartz:** Inorganic glass principally of fused silica SiO_2 , high strength, low CTE, with excellent chemical resistance. However, the drilling process involves complications.

Table 2.3: Compositions of particular reinforcements

Composition [21]	E-Glass	S-Glass	D-Glass	Quartz
SiO ₂	54.5%	65%	74.5%	99.7%
Al ₂ O ₃	14.5%	25%	0.3%	Trace Amount
CaO	17%	-	0.5%	Trace Amount
B ₂ O ₃	8.5%	-	22%	-
MgO	4.5%	10%	-	-
Na ₂ O + K ₂ O	Trace Amount	-	2.5%	Trace Amount
TiO ₂	Trace Amount	-	-	-
Fe ₂ O ₃	Trace Amount	-	Trace Amount	Trace Amount

The alternative reinforcements which were mentioned in Table-2.2 listed with their internal compositions in Table-2.3. As the SiO₂ composition increases in the fiber structure, the D_k significantly decreases due to the symmetric molecular structure, and the lower dipole polarity moment results with lower relative permittivity. However, as the SiO₂ composition increases, the mechanical properties of reinforcements become lower, and the complexity of the manufacturing process increases [21].

2.4.2 Host Matrix Selection

Most of the thermoset resins, which include high glass transition temperature, present a tendency to exhibit higher permittivity and loss due to their polar functionality [3]. Sharma et al. mentioned that ideally, materials with low dielectric constant and low loss, in a structural perspective, highly symmetric to lower the polarizability. Therefore, in Table 2.4 certain new resin systems, which can be a potential host matrix for high performance PCB applications presented.

- **FR-4 Type Epoxy Resin:** FR-4 resin is one of the most widely used resin systems in the PCB industry. The structure involves brominated epoxy resin, which reveals the fire retardancy and hardener the resin system [21].

Table 2.4: D_k and D_f values of certain resin systems

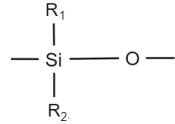
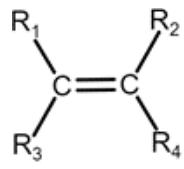
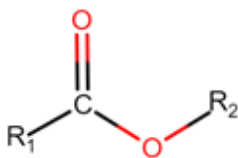
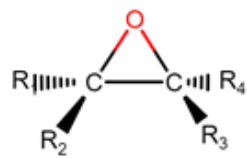
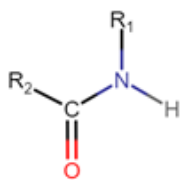
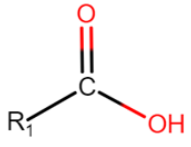
Resins	D_k	D_f
FR-4 Type Epoxy Resins	3.6	0.032
Polyimide	3.2	0.02
Cyanate Ester Based Resins	3.1	0.005
PPO Based Resins	2.9	0.004
BT Based Resins	3.1	0.003

- **Polyimide:** Polyimide resins utilize the high glass transition temperatures in order to have high thermal stability. Enhanced thermal properties exhibit the drilling process easier due to the elimination of drill smear caused by heat production [21–23].
- **PPO Based Resin:** PPO based resins are one of the candidates for high-performance PCB applications. Due to the low dielectric nature of the polymer structure and excellent heat distortion resistance.

Structural manipulation of the polymer is one of the options that altering the electrical properties of the resin system. Polymer structure can be tailored in order to present low dielectric constant and low loss. However, this tailoring process should consider the processability, thermal stability, mechanical properties. In Table-2.5, we have presented certain desirable and undesirable structures in order to obtain the provided specifications [3].

For obtaining the desired electrical properties from the proposed substrate structure, one obvious approach could be to synthesize a resin without hydroxyl or carboxyl groups. However, this approach will be impractical due to the importance of the hydroxyl groups for the adhesion property of the PCB. Popular polar polymers inherently involve hydrogen bonding moieties, which are susceptible to humidity. In response, as the polarity of the polymer changes with respect to the moisture, the dielectric constant of the materials will have a thermal dependency [3].

Table 2.5: Desirable and undesirable groups for resin matrix

Desirable groups for polymer backbone [3]		
 Aromatic	 Cycloaliphatic	 Siloxane
Reactive group for cross-linking leads to low dielectric reaction products.		
 Olefinic	$\text{HC} \equiv \text{CH}$ Acetylenic	
Groups useful in building polymer segments but detract from low D_k .		
 Ester	 Ether	 Epoxy
Groups to avoid due to their strong effects on increasing D_k .		
 Hydroxyl	 Amide	 Carboxyl

To sum up with, epoxy-based glass fiber-reinforced composites are one of the most commonly used materials in printed circuit boards due to their versatile chemistry, reasonable mechanical, thermal, adhesive and electrical properties and comparatively lower cost [24]. Facile curing process without the release of by-products, good heat and chemical resistance, low thermal expansion coefficients, high mechanical properties and adhesive strength can be counted among some of the advantages of epoxies. However, their poorer dimensional stability at high temperatures, brittleness and more importantly their relatively higher dielectric properties limit their use for high performance applications in electronics [25]. Future technologies require increased circuit densities, higher transmission speeds, smaller propagation delays and operation at higher temperatures. As a result, more reliable materials with low dielectric properties are needed [26].

Such materials include polymers like polyimides and polytetrafluoroethylene (Teflon), which are relatively expensive and harder to process [27]. Among such polymers, poly(phenylene oxide) (PPO) is a promising candidate. It is a thermoplastic having high glass transition temperature, low coefficient of thermal expansion, low flammability, low moisture absorption, excellent electrical insulation, low dielectric constant and dissipation factor and good mechanical, thermal and adhesive characteristics [26, 28].

SABIC has patented and commercialized some PPO based resins. Therefore, in this study NORYL SA9000™, a telechelic PPO oligomer with a bulky aromatic structure and phenyl methacrylate end groups used as a host matrix. Its bulky aromatic symmetrical structure and the absence of polar groups provide high free volume and low polarizability, giving lower dielectric properties which makes it viable for the high performance applications.

2.4.3 Potential Compositions

In Table 2.6, we have presented the potential laminate compositions in order to obtain proposed specifications in the motivation section. As mentioned before, E-glass, one of the most used reinforcement materials in PCB fabrication; however, it does not include the best electrical properties. One approach for decreasing the dielectric constant of the material could be increasing the SiO₂ amount in the composition however as seen in Table 2.6 as the SiO₂ proportion increased the relative cost of the product increases due to the significant reduction in mechanical properties of the substrate which is increasing the complexity of drilling.

Table 2.6: Compositions of particular reinforcements

Reinforcement/Resin	D_k	D_f	Water Uptake (mg)	Relative Cost
E-Glass/Epoxy	4.7	0.021	10	1
E-Glass/BT Resin	4.5	0.010	15	1.4
E-Glass/Polyimide	4.5	0.018	25	2.5
E-Glass/Cyanate Ester	3.9	0.003	-	5
S-Glass/Epoxy	3.6	0.003	6	6
Quartz/Polyimide	3.6	0.010	25	14
E-PTFE/Epoxy	2.8	0.012	10	10
E-PTFE/Polyimide	2.8	0.010	25	12

2.4.4 Relationship Between Dielectric Properties and GtRR

Typically, the main factor influencing the effective real part of the complex permittivity of a laminate is the variation of the glass-to-resin ratio. The dielectric properties of resin play an essential role on determining the overall dielectric properties of the laminate [3]. It is assumed that the permittivity of glass is higher than most of the epoxy and non-epoxy-based resin systems [3]. In order to alter the effective real part of the complex permittivity on a laminate, without an alteration on the chemical structures of the both building blocks, setting the glass-to-resin ratio can be a viable and simple solution.

3 Modelling

The modelling part of this study is examined under two main sections: the electromagnetic and the mechanical modelling of the proposed structures. Initially, a comprehensive description of electromagnetic modelling will be presented by introducing the proposed methods for extracting effective dielectric properties. Subsequently, the simulation setup, boundary conditions, and effective medium approximations will be evaluated.

In the second part of the modelling, the mechanical modelling of the proposed representative unit-cell will be presented by providing a comprehensive evaluation for yarn and laminate homogenization.

3.1 Electromagnetic Modelling

As mentioned in the introduction part, the design procedure of new composite material for high-performance electrical applications is based on the accurate and effective prediction of the electrical properties by considering the periodic nature of the composite structure. However, direct modeling of a fiber-woven structure inside a host matrix will require an enormous amount of computational power, conceivably violating the minimum entity dimensions of the modeled structure due to small wavelength and aspect ratio limitations. Thus, homogenization procedure or prediction of effective electrical parameters by utilizing energy-based, internal field, or scattering-based methods to overcome this challenge and predict the effective electrical properties to be utilized in the design process. Determination and modeling of a viable representative unit-cell are one of the critical components of this procedure, and it is challenging for bi, or multi-phased laminate structures [6].

In this part of the study, the homogenization-based analysis methods using periodic boundary conditions are presented. Additionally, a viable representative unit cell structure is proposed to be used for commercially available fiber reinforced with a host matrix composites to be used in high-frequency applications.

3.1.1 Effective Complex Permittivity

Since hybrid interacting micro-structures are considered as material building blocks with spatial variability and are periodically repeatable, they can be represented by an equivalent effective new material property based on Maxwell's equa-

tions. Thus, in this study, we applied a simple homogenization procedure to the internal field and energy-based approaches to extract the effective dielectric properties of a heterogeneous medium. The complex dielectric permittivity of the heterogeneous structure is extracted in single and two-level homogenization. The simulation results are compared with the common effective medium approximations and measurement results between 20 to 40 GHz.

Internal Field Based Approach: The internal field-based approach introduces the calculation of the effective dielectric properties by considering the average electric flux density and the electric field inside a medium. The effective dielectric constant is obtained by utilizing the appropriate fundamental laws presented in the background chapter. Calama et al. utilized this technique to obtain the electrostatic field solution in a porous ceramic material with fractal geometry boundaries by using the Finite Difference Method (FDM) [29]. Calama et al. include the parallel plate capacitors to perform the simulation of internal fields in a medium. The potential distributions at the edge of the representative unit-cell suggested by Peon et al. are performed by utilizing the periodic Born-Bon Karman boundary conditions [30]. Hence, there are multiple cases to utilize the internal field approach in the anisotropic heterogeneous compositions through commercial FEM software tools.

In this study, to extract the complex relative permittivity and permeability internal field approach applied by taking proper surface and volume averaging. However, as comprehensively explained in the further parts of this section, it is possible to model the heterogeneous compositions through electromagnetic simulation software by utilizing the reflection and transmission coefficients, whereas, mentioned coefficients are not sufficient to obtain the local parameters [31]. On the contrary, methods based on local area summation allow simple determination of locally effective features within the structure. In regards to the internal field approach, a heterogeneous composition medium layer that repeats a finite number of single cells along the Y-axis and by introducing periodic boundary conditions on the XZ plane can be considered [32].

The electromagnetic wave and material interaction constitutive relations are utilized, mentioned in background section (Equations: (2.1.9), (2.1.10)), to express the effective complex permittivity and the permeability. Hence, the derived version of the effective permeability in a given heterogeneous medium equation (3.1.1), for the effective complex permittivity equation (3.1.2) utilized [33].

$$\mu_0\mu_r = \frac{\langle B_x \rangle_{xyz}}{\langle H_x \rangle_{xy}} \quad (3.1.1)$$

$$\varepsilon_0\varepsilon_r = \frac{\langle D_z \rangle_{xy}}{\langle E_z \rangle_{xyz}} \quad (3.1.2)$$

Energy Based Approach: There are multiple studies done to obtain the effective dielectric properties of materials by utilizing the FEM and BIE methods to simulate the quasi-static parallel plate capacitors. Hence, to extract the real and imaginary parts of the permittivity of a composite, they measured the electrostatic energy and loss of the dielectric material [34, 35]. Therefore, in [36] the effective dielectric properties are extracted by utilizing the harmonically oscillating potential difference. Additionally, there are studies in which simulations of heterogeneous compositions with a high concentration of insulating material contents are performed by utilizing commercial FEM software tools, such as ANSYS [5] and COMSOL [37, 38].

In the further section, the determination of the simulated geometry will be examined comprehensively. A representative unit cell's sizing depends on the assumption that the maximum element dimension must be smaller than the 10% of the wavelength. Unlike the similar effective dielectric properties determination methods in the literature, in this study, the solutions of Maxwell's equations based on the quasi-static approach will not be required. The energy-based approach is primarily based on the Poynting theorem.

This method can be essentially viewed as the re-interpretation of Faraday's and Ampere's laws from the energy point of view. Mathematically, subtraction of scalar multiplications of the Faraday's law (equation (2.1.6)) with the conjugate of the magnetic field vector and the Ampere's law (equation (2.1.8)) with the electric field vector, we would end up with equation (3.1.3). E_0^2 and H_0^2 are attained by the dot product of the electric field vector and the magnetic field vector with its conjugate, respectively.

$$\nabla \cdot (\vec{E} \times \vec{H}^*) = -j\omega\mu H_0^2 + j\omega\varepsilon E_0^2 - \sigma E_0^2 \quad (3.1.3)$$

The left-hand side of equation (3.1.3) represents the power flux of the electromagnetic wave. This introduces new terms of the mean density of magnetic energy and the mean density of electric energy. Hence, the real part of the complex permittivity and permeability can be described in terms of the mean density of the electric and

magnetic energy.

$$-2j\omega(W_m - W_e) = \nabla \cdot \left(\frac{1}{2} \vec{E} \times \vec{H}^* \right) + (\sigma - \omega\varepsilon') \frac{E_0^2}{2} + (\omega\mu') \frac{H_0^2}{2} \quad (3.1.4)$$

Hence, the $(\sigma - \omega\varepsilon') \frac{E_0^2}{2} + \omega\mu' \frac{H_0^2}{2}$ term on the right hand side of the equation (3.1.4) corresponds to the amount of average power converted into heat, since the mean of the square of the trigonometric functions sine or cosine is $\frac{1}{2}$. Therefore, equation (3.1.4) primarily expresses the differential form of the complex Poynting theorem. As presented in equation (3.1.4), equations (3.1.5) and (3.1.6) are obtained to express the dielectric constant and magnetic permeability with complex vectorial functions [17].

$$\varepsilon'_r = \frac{4W_e}{\varepsilon_0 E_0^2} \quad (3.1.5)$$

$$\mu'_r = \frac{4W_m}{\mu_0 H_0^2} \quad (3.1.6)$$

On the other hand, the imaginary part of the complex permittivity is extracted from the heat transfer equation. That will be utilized to determine the power loss that is delivered to the representative unit cell. Therefore, governing of the heat transfer phenomena is presented as in equation (3.1.7) [17].

$$Q_{em} = \rho c_p \frac{\partial T}{\partial t} - \nabla \cdot \kappa \nabla T \quad (3.1.7)$$

where Q_{em} denotes the heat generation, ρ is the density, κ is the thermal conductivity, and c_p is the specific heat capacity of the representative unit element. For this modal, Q_{em} is the representation of the electromagnetic power dissipation. Therefore, the heat generation process due to power transfer extracted by the equation (3.1.8).

$$Q_{em} = (\sigma + \omega\varepsilon'') \frac{E_0^2}{2} \quad (3.1.8)$$

As a result, the final form of the imaginary part of the complex permittivity is presented as in equation (3.1.9).

$$\varepsilon_r'' = \left[\frac{2Q_{em}}{\varepsilon_0\omega E_0^2} \right] - \left[\frac{\sigma_{eff}}{\varepsilon_0\omega} \right] \quad (3.1.9)$$

Scattering Based Approach: Meta-materials is a common research area where the calculation of the effective dielectric parameters is of great importance through a scattering-based approach. The scattering-based approach provides the effective dielectric properties of the sample by calculating the reflection and transmission wave passing through the heterogeneous composition. Hence, Weiland et al. utilized commercially available CST microwave studio software to extract [39]. The calculation of this software is based on the finite integration technique by utilizing the ideal boundary conditions. Additionally, Liu et al. calculated the complex effective dielectric properties of the planar composite material which contains conductive fibers by using commercially available High Frequency Structure Simulator (HFSS) software, as a Finite Element Method (FEM) software [40].

3.1.2 Effective Medium Approximations

Classical mixing rules (CMR) and effective medium approximations (EMA) mainly depend on the energy differences requiring simple calculation rather than calculating the direct energy. EMA's and other related approaches mainly depend on the composite structure's physical model and the ratio between their building blocks (GtRR). The most common examples of EMA's are utilized by the dielectric permittivity and the conductivity of the laminate structures [41]. The accuracy of these approaches depending on the choice of representative unit cell element dimensions, permittivity contrast, and fraction between building blocks of the laminates. The visual implementation steps of effective medium approximations are presented in Figure 3.1.

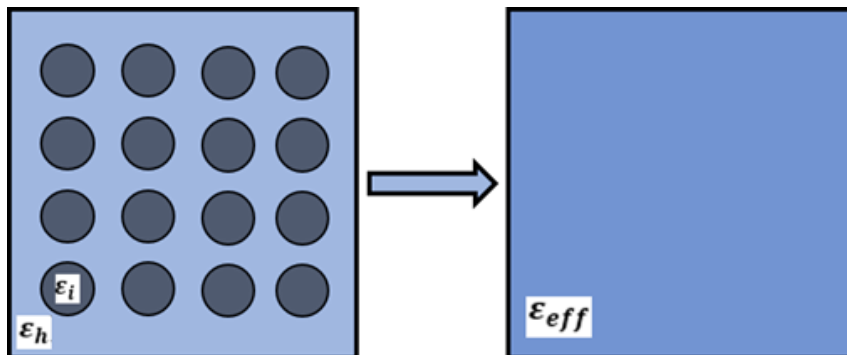


Figure 3.1: Simple homogenization procedure of bi-phased composite structure: ε_i denotes the circular inclusions of the 2D host matrix, ε_h describes the permittivity of the host matrix, and ε_{eff} denotes the macroscopic permittivity response of the heterogeneous medium.

where, ε_i denotes the circular inclusions of the 2D host matrix, ε_h describes the permittivity of the host matrix. The evaluation of both internal and energy-based methods are done by the most common effective medium approximations as stated below.

Maxwell-Garnet Approximation: Maxwell-Garnett (MG) approximation is one of the most famous EMA used for predicting the dielectric properties of the heterogeneously composed media. MG approximation takes into consideration of the induced polarization that occurs under a uniform external electric field. This approximation is initially implemented on heterogeneous structures that include spherical inclusions inside a host matrix. Therefore, the provided version of the Maxwell-Garnett approximation considers that the introduced inclusion into the host matrix is cylindrical shaped and stretches infinitely inside the host matrix [7]. Therefore, the ε_{eff} (effective permittivity) of a heterogeneous medium calculated based on MG approximation in equation (3.1.10) [7].

$$\varepsilon_{eff} = \varepsilon_h + 3f\varepsilon_h \frac{\varepsilon_i - \varepsilon_h}{\varepsilon_i + 2\varepsilon_h} \quad (3.1.10)$$

where, ε_{eff} is the effective electrical permittivity of the total medium. ε_h represents the electrical permittivity of the resin matrix surrounding the fillers or the reinforcement structures. Therefore, ε_i is representing the electrical permittivity of the introduced inclusions. Finally, f denotes the volume fraction of the medium.

Symmetric Bruggeman Approximation: Another famous effective medium approximation is the Bruggeman Approximation (SB), which takes into consideration the effective medium theory as in Maxwell-Garnett approximation. In comparison, SB approximation utilizes the symmetry between the introduced inclusions and the host matrix. Hence, asymmetrical Bruggeman's theory is utilized to determine the inconsistently shaped inclusions inside the host matrix [6]. However, one of the estimation problems about the SB approximation is that it overestimates the effective permittivity of the heterogeneous medium when the volume fractions among the host matrix and inclusions are small with respect to the MG approximation. SB approximation is presented in equation (3.1.11) [7].

$$\varepsilon_{eff} = \frac{1}{4} \left[3f(\varepsilon_i - \varepsilon_h) + 2\varepsilon_h - \varepsilon_i + \sqrt{(1 - 3f^2)\varepsilon_i^2 + 2(2 + 9f - 9f^2)\varepsilon_i\varepsilon_h + (3f - 2)^2\varepsilon_h^2} \right] \quad (3.1.11)$$

where, ε_i denotes the permittivity of the inclusions, ε_h denotes the permittivity of the host matrix, and f describes the volume fraction ratio among the inclusions and the host matrix.

Looyenga Approximation: This study's last effective medium approximation is the Looyenga approximation; with respect to the initial two approximations, the Looyenga approximation is not commonly used as the MG and the SB approximations. However, the distinctive property of the Looyenga approximation with respect to the MG and the SB approximations is that the approximation can be modified with regards to inclusion shape by altering the variable "A" as stated in equation (3.1.12). In this study, the variable $A=2$ due to inclusion shape inside host matrix [42].

$$\varepsilon_{eff} = \left[(\varepsilon_i^{1/A} - \varepsilon_h^{1/A})f + \varepsilon_h^{1/A} \right]^A \quad (3.1.12)$$

where, variable "A" describes the depolarization factor, ε_h denotes the permittivity of the host matrix and, ε_i denotes the permittivity of the inclusions [42].

3.1.3 Simulation Setup and Results

In this section, the simulation setup and simulation results are examined comprehensively. All simulations are examined in terms of boundary conditions, representative unit cell determination, the difference of single and two-level homogenization, post-processing, and finally, the simulation and effective medium approximation results compared, respectively.

Boundary Conditions

In this study, simulations are conducted via the commercially available COMSOL multi-physics software. Simulations are conducted under the Electromagnetic waves and Frequency domain module of the COMSOL multi-physics. Simulations under this module are solved through the wavelength domain by utilizing parametric sweep. In order to determine the computational region wave equation defined on the total structure as presented in Figure 3.2. Based on both energy-based and internal field approaches, a material layer that repeats a finite number of single cells along the Z-thickness dimension and has an infinite periodic extension in the XY plane can be considered. The incident wave is defined along the Z-axis with vector \mathbf{k} . The X-axis and Y-axis define the E-field and H-field, respectively. Therefore, the periodic boundary conditions (PBC) are defined on the XZ and YZ surfaces of the computation region to represent the periodic structure of the E-glass fabric, as shown in Figure 3.2. Thus, the type of periodicity of the periodic boundary condition is determined as Floquet periodicity. Both sides of the unit cell are defined by the air domain. The dimensions of the air domains are determined with respect to the introduced wavelength. The port type for the top and bottom of the air domains is selected as periodic to introduce the excitation wave into the system by the port boundary conditions. The wave excitation was introduced into the system via port 1, and port 2's wave excitation was disabled to exclude the back reflection from the system.

Due to the complex nature of the geometry, which is explained comprehensively in the further sections, automatic meshing was not suitable for this study. Therefore,

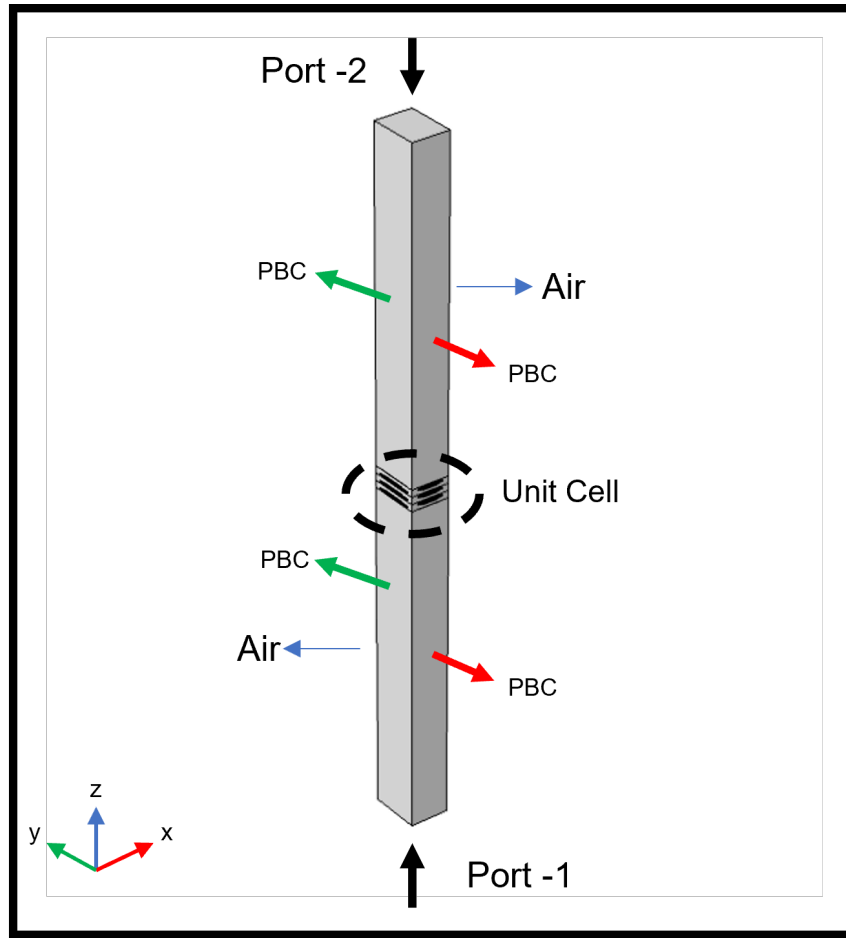


Figure 3.2: Determined simulation setup and boundary conditions for single level homogenization at 20 GHz

mesh assignment was done in the user-defined mode by utilizing the mesh module's free triangular, distribution, and copy features; the number of elements defined by the assigned mesh was around the magnitude of order $10^6 - 10^7$ elements in these simulations.

Representative Unit Cell Determination

In advance of the determination of the representative unit cell, it is required to enhance the geometrical knowledge about the reinforcement types. Hence, this study utilizes 106 and 1080 types of E-Glass fiber fabric to reinforce the host matrix. Therefore, the generic representation of the E-Glass fiber fabric's dimensions are denoted as shown in Figure 3.3. The vertical fiber bundles are called "warp" and horizontal fiber bundles are called "weft". The provided reinforcement dimensions in Table 3.1 will have vital importance in the determination of the unit cell. The numerical values of X_3 and Y_3 determine X and Y dimensions of the unit cell size. Thus, X_1 and Y_1 determine the minimum thickness of the unit cell.

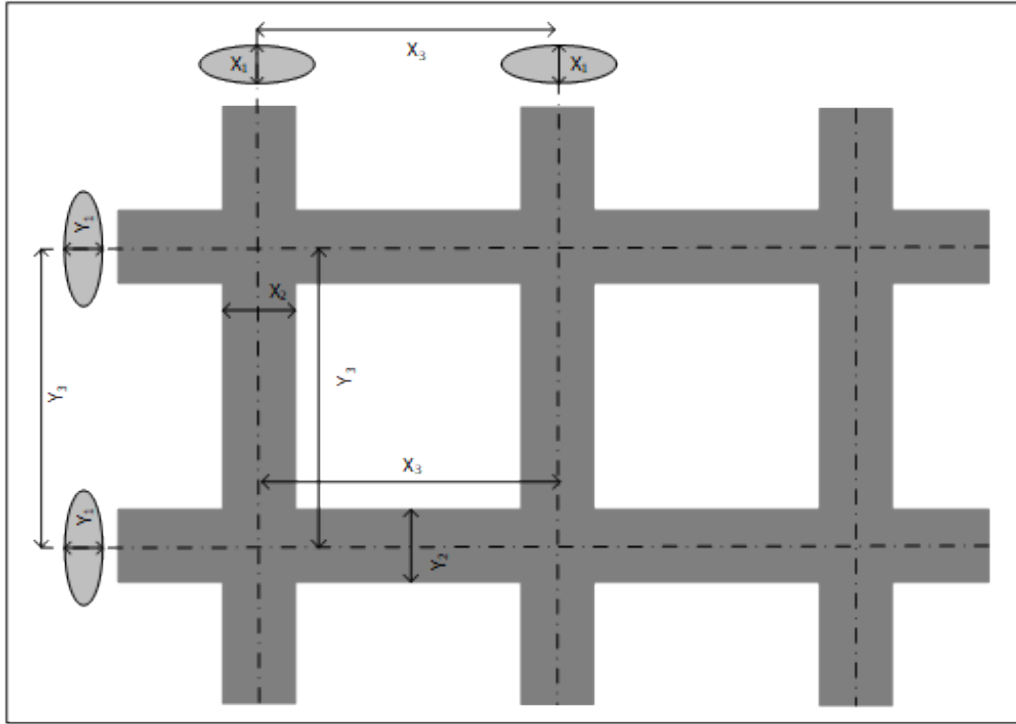


Figure 3.3: Illustration of the generic E-Glass fiber fabric's denotations of the dimensions

Optical microscopy images of the 106 and 1080 types of E-Glass fiber fabric are presented as shown in 3.4. In ideal fabrication conditions, due to X_1 and Y_1 , the minimum thickness of the composites manufactured with 1080 type of E-Glass fiber fabric is larger than the composites that is manufactured with 106 type of E-Glass fiber fabric. Eventually, the composite thickness variation has a significant effect on the volume fraction ratio of the fiber. The volume fraction is also known as the "Glass to Resin ratio". 106 and 1080 types of E-Glass fiber fabrics are common reinforcement types for high-performance applications. As presented in Figure 3.4, 1080 and 106 types of E-Glass fabric have a large intersection gap. These gaps will provide an impedance alteration on the copper transmission lines and will severely affect the signal. Therefore, in high-speed applications that utilize E-Glass fiber fabrics are uniformly distributed along the X and Y-axis. In high-frequency applications, impedance alteration along the transmission line is important. However, 106, 1080, and the enhanced derivatives of E-Glass were utilized in the high frequency and antenna applications.

To determine the representative unit cell dimensions, there should be considered two distinct contributions. As stated at the beginning of this section, the initial contribution was introduced by the dimensional properties of the E-Glass fabric and how well its represented their periodic nature.

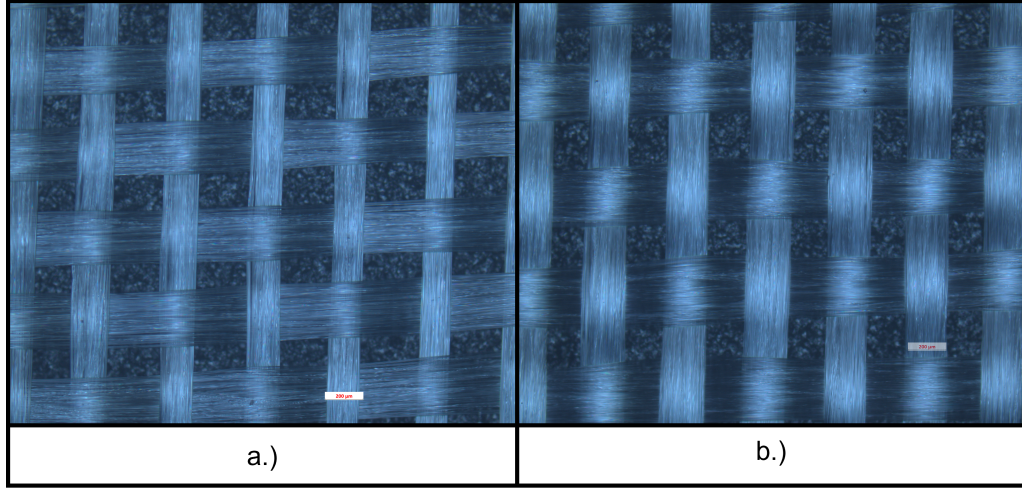


Figure 3.4: a.)Optical microscopy images of a.)106 type of E-Glass fiber fabric. b.)1080 type of E-Glass fiber fabric.

The second contribution is introduced by the irradiated wavelength into the computational region, where the wavelength of the irradiation is longer than the dimensions of the inclusions. There are two different proposed representative unit cell that exists in this study. The proposed representative unit cell dimensions are optimized to make the final composite structure suitable for working in various frequency bands.

Both the homogenization and the effective medium theories to hold, for composites with periodic unit cells, a representative unit cell structure's maximum length should not exceed $\lambda/10$ in size. Therefore, the representative unit cell's dimensions should not exceed $750 \mu m$ at center frequency of 40 GHz. The illustration of the representative unit cell dimensions under the effects of both wavelength and fiber dimensions are presented in Figure 3.5. Figure 3.5a determines a generic E-Glass fiber fabric reinforced composite's representative unit cell geometry, and this representation will be viable in terms of periodic nature of the fabric and is viable up to 20 GHz. Figures 3.5b and 3.5c determine the viable unit cells that include both irradiated wavelength and periodicity conditions that are viable approximately till 50 GHz and 100 GHz, respectively.

In this study, two distinct representative unit cell types were proposed, they

Table 3.1: Dimensions of reinforcement as a E-Glass fiber fabric

Glass Fabric	$X_1 (\mu m)$	$X_2 (\mu m)$	$X_3 (\mu m)$	$Y_1 (\mu m)$	$Y_2 (\mu m)$	$Y_3 (\mu m)$
106	25.4	121.92	469.9	15.24	259.08	523.24
1080	40.64	208.28	431.8	27.94	307.34	568.96

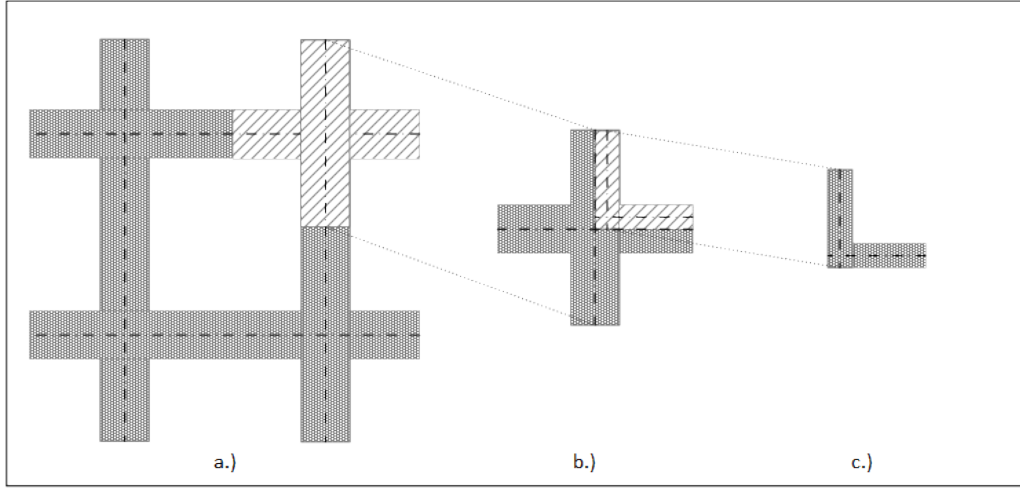


Figure 3.5: Illustration of the representative unit cell dimensions with respect to the introduced wavelength into the system. Generic representative unit element sizing till, a.)20 GHz, b.)50 GHz, c.)100 GHz

are plane weave representation and the bundle weave representation. Plane weave representation ignores the cylindrical nature of the single fibers. Therefore, the proposed plane weave representation is ambiguous in terms of the computational region's aspect ratio due to the increment in the assigned mesh's complexity. The proposed plane weave type of unit cell is presented as in Figure 3.6. The total and local electric field distributions are presented in Figures 3.6a and 3.6b respectively. The assigned mesh into the plane weave representation geometry is presented in Figure 3.6c. Due to the low quality of the assigned mesh, which is in between two consecutive fiber layers, the stability of the parametric simulation is degraded in various frequency points.

Subsequently, the cylindrical nature of fibers is taken into consideration by bundle weave representation, where the simulation geometry includes all fibers in a representative unit cell. The number of fibers in the warp and weft directions are determined by the SEM images of the 106 and 1080 types of E-Glass fiber fabrics. Therefore, the number of elements in the computational region is increased exponentially with respect to the plane weave representation. However, mesh distribution and simulation stability are enhanced compared to the plane weave representation. The total and local electric field distributions are presented in Figures 3.7a and 3.7b. The mesh assignment into the bundle weave representation is presented in Figure 3.7c.

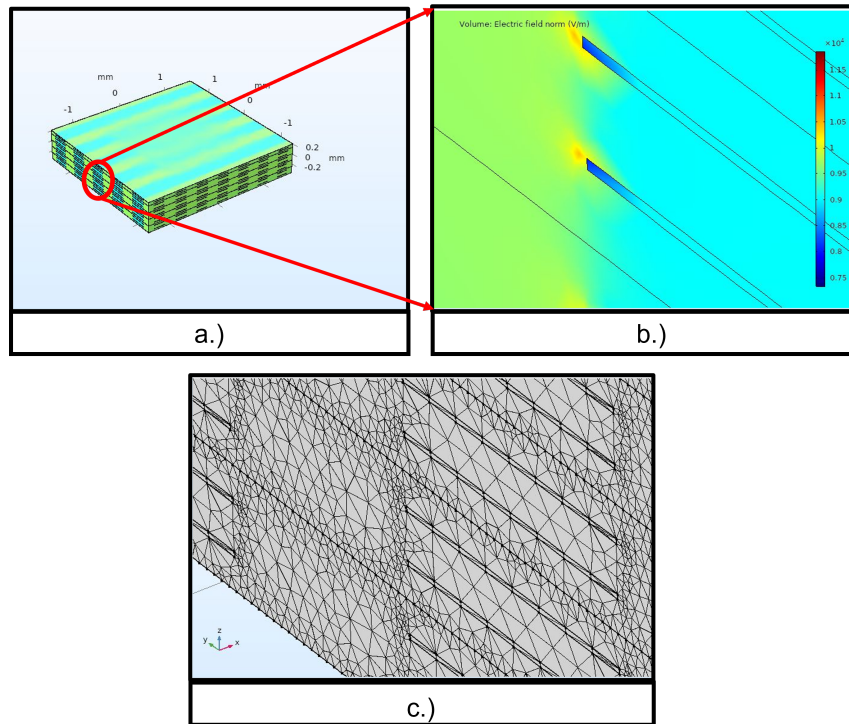


Figure 3.6: Simulation setup of the plane wave representation, a.)Total E-field distribution, b.)Local E-field distribution, c.)Assigned mesh at 800 MHz

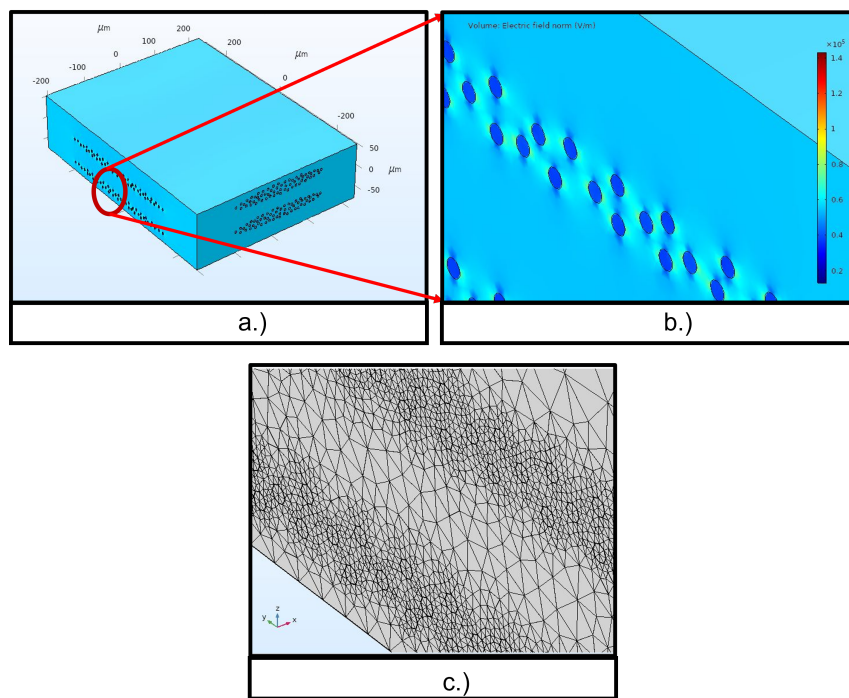


Figure 3.7: Simulation setup of the bundle wave representation, a.)Total E-field distribution, b.)Local E-field distribution, c.)Assigned mesh at 20 GHz

Single & Two Level Homogenization with Bundle Weave Representation

Bundle weave representation is utilized to extract the effective dielectric properties of the 106, and 1080 types reinforced composite structures with single and two-level homogenization procedures. As mentioned in the previous section, bundle weave representation employs the cylindrical nature of fibers. However, the cylindrical representation of fibers increases the computational power cost of the bundle weave representation. Therefore, to decrease the computational load, the homogenization procedure is separated into two levels, hence reduction of the simulation time and the number of elements can be accomplished.

Single level homogenization is applied to the 106, and 1080 types of E-Glass reinforced composite structure. The simulation steps of the single level homogenization are presented in Figure 3.8, where, Figure 3.8a describes the bundles of 106 type E-Glass on XY plane which, are located in the host matrix, and Figure 3.8b presents the target region to extract the effective dielectric properties.

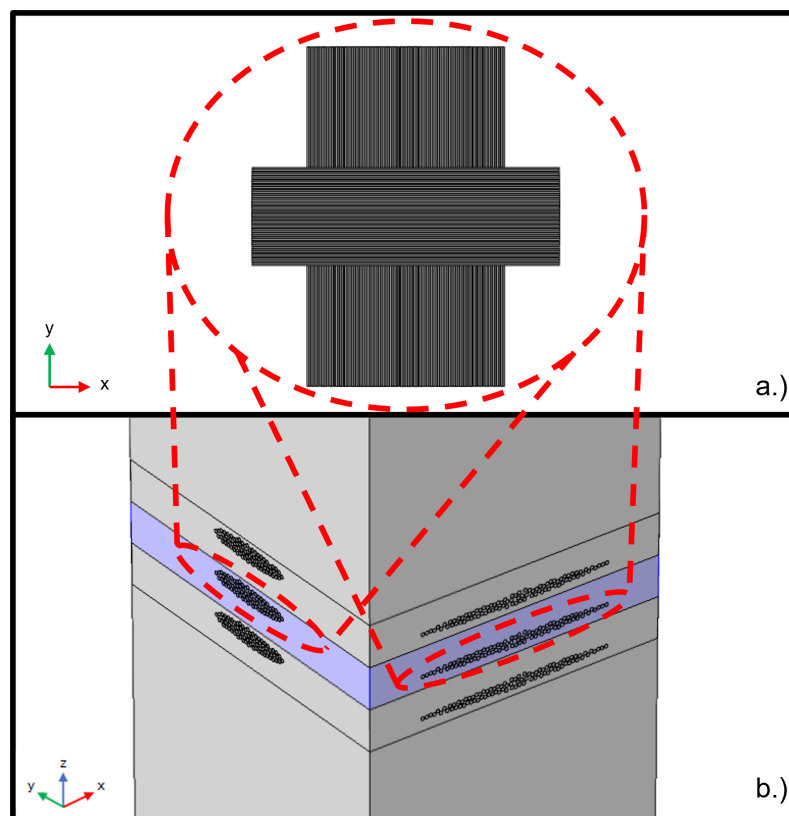


Figure 3.8: Single level homogenization procedure with the bundle weave representation. a.)Determined fiber bundles for 106 type E-Glass fabric. b.)Total geometry of the simulation setup and homogenized region at 40 GHz.

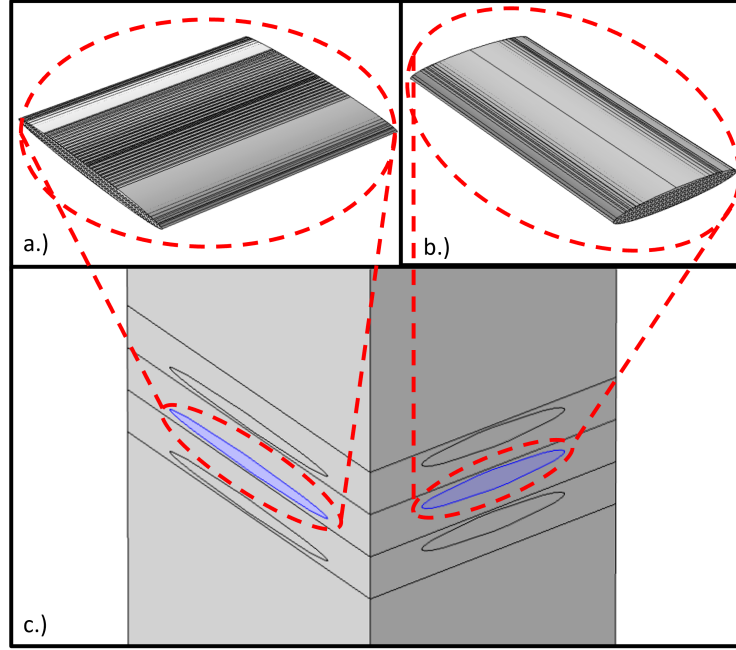


Figure 3.9: Two level homogenization procedure with the bundle weave representation. a.)Determined fiber bundles for warp direction 1080 type E-Glass with host matrix. b.)Determined fiber bundles for weft direction 1080 type E-Glass with host matrix. c.)Second level homogenization

Two-level homogenization is applied to the 1080 type of E-Glass due to having a larger cross-section area in the weft and warp-directed bundles with respect to the 106 type E-Glass. Hence, the number of fibers per unit cell approximately increased by 50% and directly affected the computation time. Initially, the homogenization procedure is applied only on the fiber bundles with a host matrix as presented in Figures 3.9a and 3.9b. Furthermore, extracted effective dielectric properties from Figures 3.9a and 3.9b are inserted into the elliptically represented bundles in Figure 3.9c. As a result, the total composite structure's effective dielectric properties are extracted.

Subsequently, simulation results presented in Figure 3.10 and Figure 3.11 were obtained by utilizing the single level homogenization for 106 type of E-Glass fabric. In Figure 3.10 and 3.11, the effective dielectric constant and dissipation factor are presented and are compared with the effective medium approximations from 20 GHz to 40 GHz, respectively. The obtained effective medium approximation results depend on the measurement results of the inclusions and the host matrix from 20 to 40 GHz. As a result, the extracted effective dielectric constant and dissipation factor through FEM simulations present a good agreement among each other. Furthermore, the dissipation factor extracted through energy based approach coincides with Maxwell-Garnett's and Looyenga's effective medium approximations.

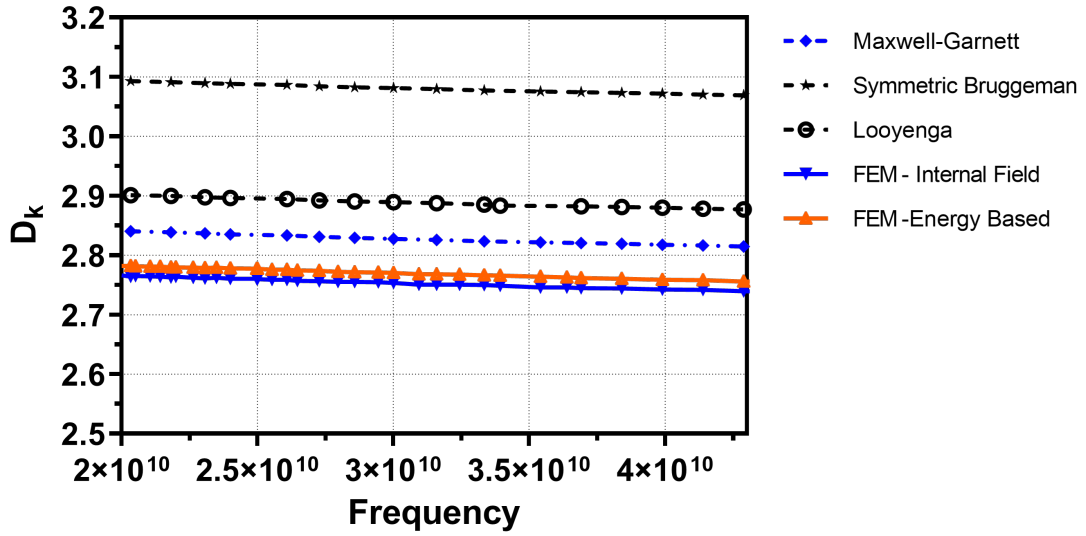


Figure 3.10: Simulation results of effective dielectric constant, via internal field and energy based approaches under single level homogenization procedure compared with common effective medium approximations for E-Glass(106)+PPO composition.

Consequently, single and two-level homogenization procedures were applied on the internal field and energy-based approaches in the proposed simulations. The effective dielectric constant and dissipation factor results are presented in Figure 3.12 and Figure 3.13 respectively.

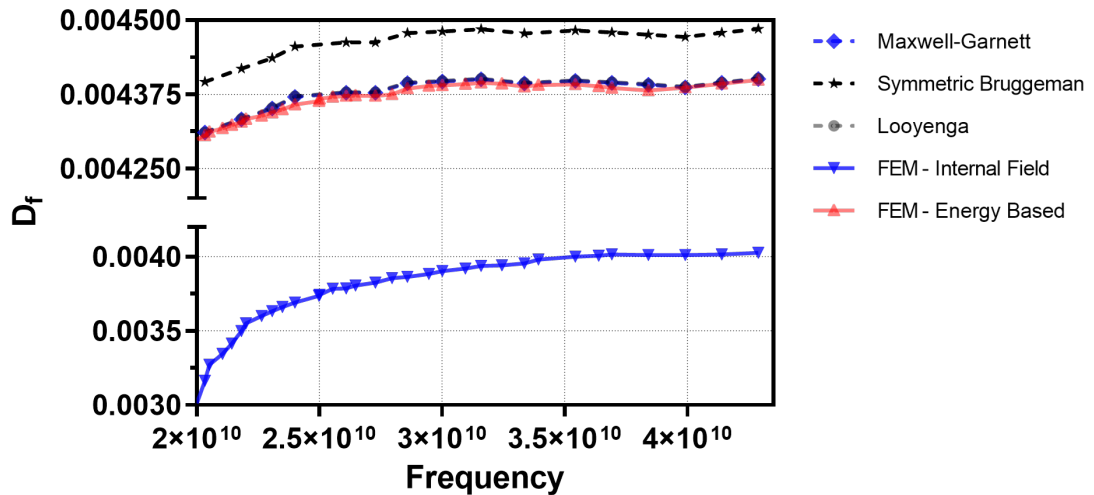


Figure 3.11: Simulation results of effective dissipation factor, via internal field and energy based approaches under single level homogenization procedure compared with common effective medium approximations for E-Glass(106)+PPO composition.

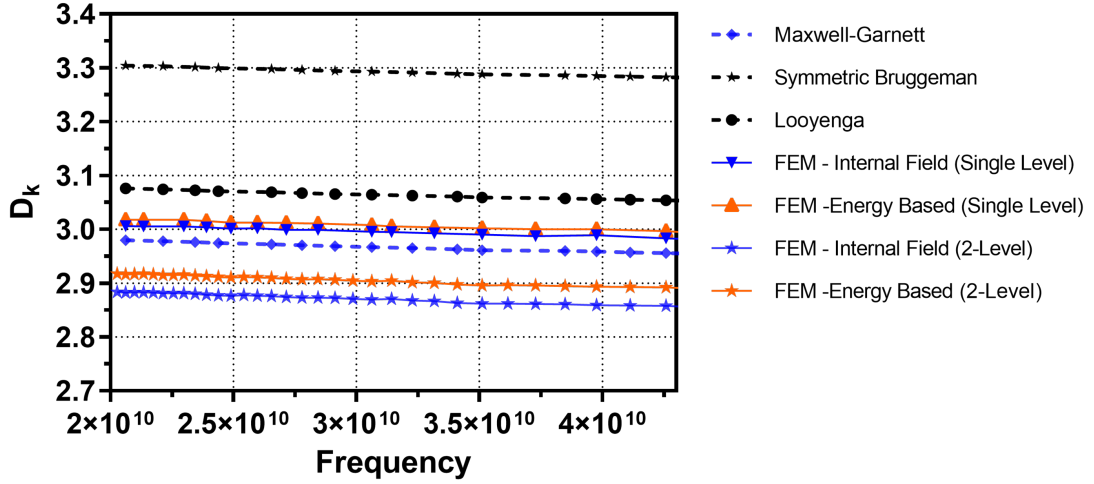


Figure 3.12: Simulation results of effective dielectric constant, via internal field and energy based approaches under single and two level homogenization procedures compared with common effective medium approximations for E-Glass(1080)+PPO composition.

The effective dielectric constant results extracted by the single and two-level homogenization procedures are in coherence with each other. However, the SB effective medium approximation overestimates the effective dielectric constant for both 106 and 1080 reinforced compositions. Furthermore, the effective dissipation factor results obtained by the energy-based approach coincide with each other in both single and two-level homogenization procedures. Hence, these results are strongly coherent with the MG and Looyenga's effective medium approximations.

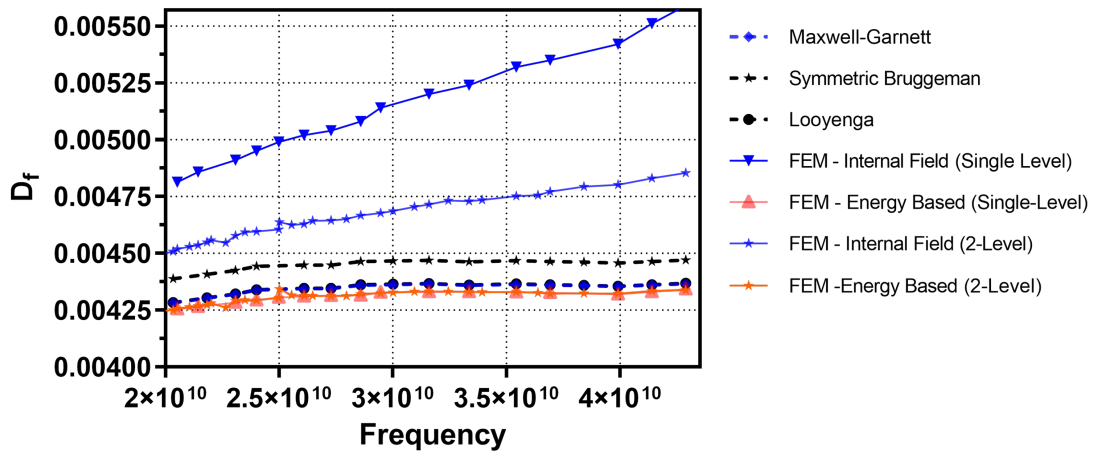


Figure 3.13: Simulation results of effective dissipation factor, via internal field and energy based approaches under single and two level homogenization procedures compared with common effective medium approximations for E-Glass(1080)+PPO composition.

Post-Processing

As mentioned in previous sections of the modelling chapter, the effective dielectric properties are obtained by applying energy-based and internal field approaches. However, by default, the output data format of these simulations does not satisfy the homogenization conditions. Therefore, to extract the effective dielectric properties of the non-homogeneous medium, post-processing required on parameters, such as mean density of electric energy (W_e), electric field norm (E_0) and relative components of electric field and displacement field.

In the post-processing procedure of the energy-based approach, the volume averaging requires extracting the effective mean density of electric energy (W_e) and the effective electric field norm (E_0) on the target region, which are shown as the blue region in Figure 3.8.

The homogenization procedure satisfied by the volume-averaged parameters and the effective ϵ'_r can be obtained by the insertion of volume-averaged parameters into equation (3.1.5). The same volume averaging procedure is viable for the effective ϵ''_r by using equation (3.1.9).

Subsequently, the post-processing procedure of the internal field approach differentiates from the energy-based approach in terms of averaging conditions. Therefore, the homogenization procedure of the internal field can be described as volume/surface averaging [33]. The real and imaginary parts of the effective complex permittivity are extracted by the ratio of the surface averaged displacement field to the volume-averaged electric field. For instance, the target substrate is excited by a Y-polarized electric field, the surface averaging of displacement field has to be applied on the surface that is perpendicular to the electric field. Thus, the ratio of the averaged Y-component of the displacement to the volume-averaged electric field is attained. The real and imaginary part of the above ratio forms ϵ'_r and ϵ''_r , respectively, as shown in equation (3.1.13) and (3.1.14).

$$\epsilon'_r = \text{real} \left[\frac{\langle D_y \rangle_{xz}}{\langle E_y \rangle_{xyz} \epsilon_0} \right] \quad (3.1.13)$$

$$\epsilon''_r = \text{imag} \left[\frac{\langle D_y \rangle_{xz}}{\langle E_y \rangle_{xyz} \epsilon_0} \right] \quad (3.1.14)$$

Consequently, the numerical computation of the effective complex permittivity done by using MATLAB is presented in Appendix D.

3.2 Mechanical Modeling

The mechanical simulations of the composites are widely utilized in both the literature and the industry. Therefore, the effective mechanical properties of the composites can be extracted in multi-level homogenization techniques as similar to the two-level homogenization procedure that we have conducted in section 3.1.3 to extract the effective dielectric properties. The two-level homogenization technique in mechanical simulations can be described as Yarn and Laminate homogenization separately. However, in this study, we will only introduce the Yarn homogenization technique. The mechanical response of laminates is orthotropic, therefore, to extract the effective mechanical properties, particularly the determination of elastic orthotropic behaviors of the fiber weave and resin compositions examined in literature by using experimental and numerical methods [43]. Subsequently, due to the simplicity of the unit cell geometry determination, the well-known Mori-Tanaka technique was introduced into the simulation environment. Mori-Tanaka technique utilizes the unit cell as a single fiber and host matrix composition to model the yarn behavior of the composite structure. Thus, yarn behavior is primarily composed of two phases, host matrix, and fiber, and is based on the development of the finite element model of composite's representative volume element (RVE).

Consequently, in the literature most of the published mechanical measurements were examining the epoxy type resins. Therefore, in yarn homogenization modelling the host matrix assumed as Epoxy based host matrix instead of PPO based host matrix.

3.2.1 Yarn Homogenization

The yarn homogenization is the first level homogenization, to determine the effective mechanical properties of the proposed composite structure. In order to determine the yarn response of the structure we have utilized the homogenization method proposed by the Stevens et al. [44]. Thus, the effective mechanical properties of the material extracted from a single unit cell of the yarn. Hereby, it is possible to determine the transverse isotropic behavior of fibers in a host matrix can be determined by the equation (3.2.1) .

$$\varepsilon = S : \sigma \tag{3.2.1}$$

where, S denotes elastic 'compliance' tensor and called as compliance matrix and it is the inverse of the D-matrix or called as the elasticity matrix. Therefore, the orthotropic behaviour of the model can be described by the Hooke's law as presented below .

$$\begin{pmatrix} \varepsilon_{11} \\ \varepsilon_{22} \\ \varepsilon_{33} \\ 2\varepsilon_{12} \\ 2\varepsilon_{13} \\ 2\varepsilon_{23} \end{pmatrix} = \begin{bmatrix} \frac{1}{E_1} & -\frac{\nu_{12}}{E_1} & -\frac{\nu_{13}}{E_1} & 0 & 0 & 0 \\ -\frac{\nu_{12}}{E_1} & \frac{1}{E_2} & -\frac{\nu_{23}}{E_2} & 0 & 0 & 0 \\ -\frac{\nu_{13}}{E_1} & -\frac{\nu_{23}}{E_2} & \frac{1}{E_3} & 0 & 0 & 0 \\ 0 & 0 & 0 & \frac{1}{G_{12}} & 0 & 0 \\ 0 & 0 & 0 & 0 & \frac{1}{G_{13}} & 0 \\ 0 & 0 & 0 & 0 & 0 & \frac{1}{G_{23}} \end{bmatrix} \begin{pmatrix} \sigma_{11} \\ \sigma_{22} \\ \sigma_{33} \\ \sigma_{12} \\ \sigma_{13} \\ \sigma_{23} \end{pmatrix} \quad (3.2.2)$$

Subsequently, the modelled structure simulated under the solid mechanics module in COMSOL Multiphysics software, by introducing the cell periodicity boundary conditions to express the periodic nature of the composite structure. Thus, to extract the mechanical response of the modelled unit cell "load groups" defined in all the directions provided by the equation (3.2.2). The simulation geometry presented as in 3.14 by introducing the 1080 type E-Glass and Epikote-828 host matrix.

Therefore, the comparison of the proposed model done with the effective mixture rules. The mixture rule commonly known method to predict the effective material properties of composite structures. The calculation of the Mixture rule depends on the mechanical material properties of each components and their volume fractions. Thus, the longitudinal Young's modulus of the unit cell can be calculated

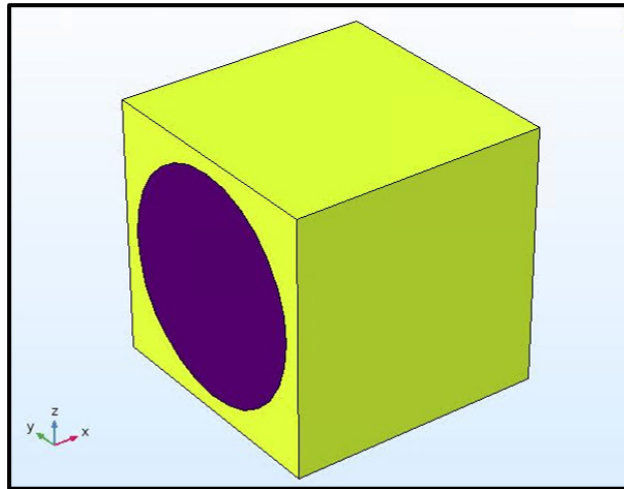


Figure 3.14: Developed model to extract the effective mechanical properties of the unit cell

Table 3.2: Comparison of cell periodicity yarn homogenization with mixture rules results

Material Property	Yarn Homogenization	Mixture Rule
Longitudinal Young's Modulus (E_1/E_m)	18.8	17.7
Transverse Young's Modulus (E_2/E_m)	7.5	2.5
Volume fraction ratio	0.7	0.7

when the applied force direction same as the direction of fibers (E_1) presented in equation (3.2.3).

$$E_1 = E_1V_f + E_mV_m \quad (3.2.3)$$

where, E_m and E_1 denote Young's modulus of host matrix and fiber in longitudinal. V_f and V_m denote volume fractions of the fiber and host matrix. However, the transverse Young's modulus of the unit cell can be calculated when the applied force is perpendicular to the fiber orientation (E_2) and presented in equation (3.2.4)

$$\frac{1}{E_2} = \frac{V_f}{E_{2f}} + \frac{V_m}{E_m} \quad (3.2.4)$$

Additionally, Poisson's ratio and Shear modulus can be described with mixture rule, presented in equations (3.2.5) and (3.2.6) respectively.

$$\nu_{12} = \nu_{12f}V_f + \nu_mV_m \quad (3.2.5)$$

$$\frac{1}{G_{12}} = \frac{V_f}{G_{12f}} + \frac{V_m}{G_m} \quad (3.2.6)$$

Consequently, cell periodicity based Yarn homogenization model and effective mixture rule results of compared as in Table 3.2. The presented longitudinal and transverse Young's modulus are normalized with the Young's modulus of the host matrix. The last step of the Yarn homogenization is to calculate the D-matrix which contains the effective mechanical material properties of the modeled unit cell. The obtained D matrix values presented below. The Young's modulus and shear modulus and Poisson's ratios obtained from the D matrix will be converted into the compliance matrix and it will be provided as the input of the second level homogenization also, called as laminate homogenization.

$$D = \begin{bmatrix} 1.78E - 11 & 1.31E - 10 & 1.31E - 10 & 0 & 0 & 0 \\ 1.31E - 10 & 4.27E - 11 & 1.63E - 10 & 0 & 0 & 0 \\ 1.31E - 10 & 1.63E - 10 & 4.27E - 11 & 0 & 0 & 0 \\ 0 & 0 & 0 & 1.55E - 10 & 0 & 0 \\ 0 & 0 & 0 & 0 & 2.29E - 10 & 0 \\ 0 & 0 & 0 & 0 & 0 & 2.29E - 10 \end{bmatrix} \quad (3.2.7)$$

4 Characterization

The fabricated composites and their building blocks are characterized in terms of their dielectric properties by using different methods at a diverse range of frequencies. Fabry Perot Open Resonator (FPOR) and Split Post Dielectric Resonator (SPDR) techniques have been utilized in this study to extract the effective dielectric properties of the fabricated composites. Furthermore, the modelling results of the composite structures compared with the measurement results obtained by the FPOR technique in between 20 GHz to 40 GHz. Subsequently, effective dielectric constant and dissipation factor extracted with a more precise method of SPDR. Consequently, the final effective dielectric constant and dissipation factor extraction method proposed and design and simulation procedure comprehensively explained in Section 4.4.

4.1 Fabry Perot Open Resonator(FPOR) Measurement

The characterization of low loss materials have been made by the FPOR setup between 20 GHz to 40 GHz. FPOR is an automated resonance measurement device that creates a viable measurement environment for low-loss dielectric materials. FPOR setup contains silver plated Gaussian mirrors top and bottom side of the resonator with a highly precise sliding stage to provide a transition between the TEM modes in Z-Axis of the open resonator, as the cross-sectional illustration and realized measurement setup was presented in Figure 4.1 and Figure 4.2 [45]. The measurement procedure initiated with the measurement of unloaded resonance frequency and unloaded quality factor of the open resonator and continues with the insertion of the material under test (MUT) into the resonator.

Theoretically, the closest location of the minimum electric field could be determined, so identify the relevant modes the MUT has been shifted to the above mentioned position from the center of the open resonator where the electric field is maximum. Hence, the identification of the first mode of interest completed the MUT shifted back to the open resonator's center and recorded resonance frequency and quality factor simultaneously. The extracted results were converted by the comparison of a look-up table, which was previously generated by the EM model of the empty FPOR, to the dielectric constant and dissipation factor [45]. The resonance frequency and the quality factor of the FPOR were extracted through Keysight-PNA M5224A till 43.5 GHz.

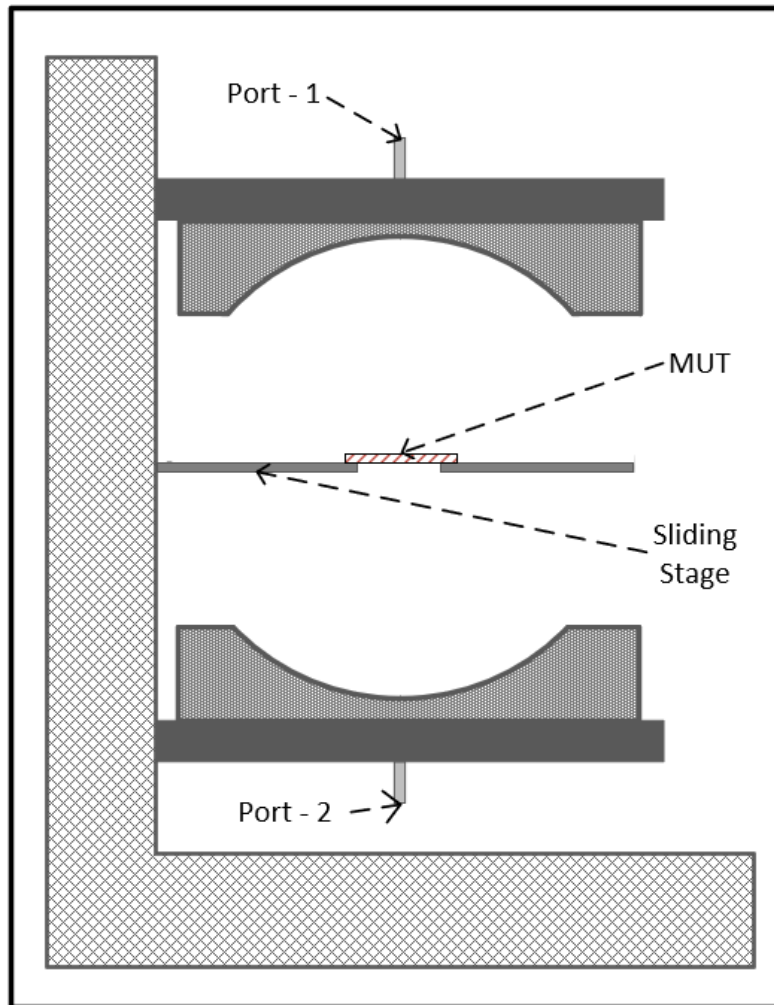


Figure 4.1: Cross-sectional illustration of the Fabry Perot Open Resonator.

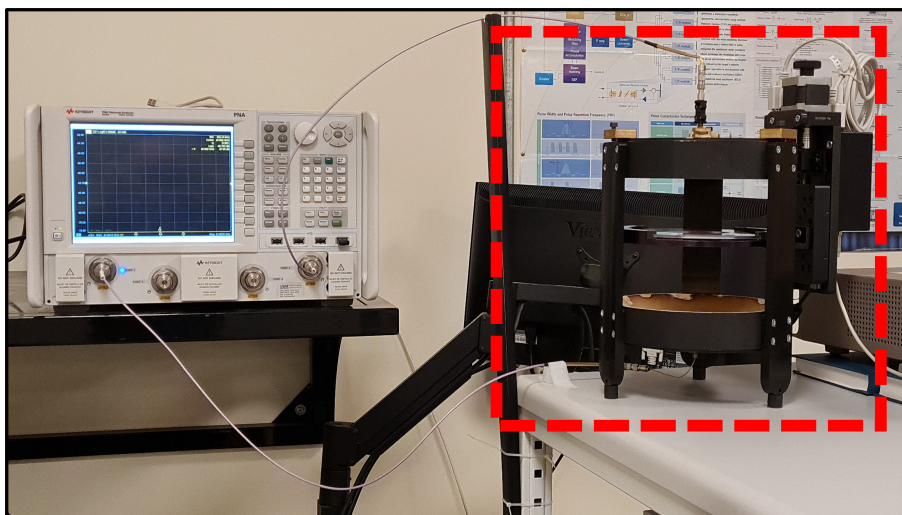


Figure 4.2: The realized measurement setup between 20 GHz to 40 GHz for FPOR measurements.

Subsequently, the proposed modelling setups were evaluated by the measurement results through the FPOR measurement between 20 GHz to 40 GHz. Therefore, the comparison of E-Glass(106)+PPO composition's modelling and measurement results presented in Figure 4.3 and Figure 4.4.

The 106 reinforced composition's estimated effective dielectric constant is larger with respect to FPOR measurement results. The distinction between the simulation and measurement results depends on the thickness variation of the targeted measurement region due to the dependence of the dielectric constant on thickness. Therefore, as mentioned above, the MUT holder shifts automatically when the transition from the minimum electric field to the maximum electric field locations occurs. Hence, the automatic shifting procedure takes into consideration the thickness of the MUT. On the other hand, the measurement results and modelling results are in coherent in terms of the dissipation factor.

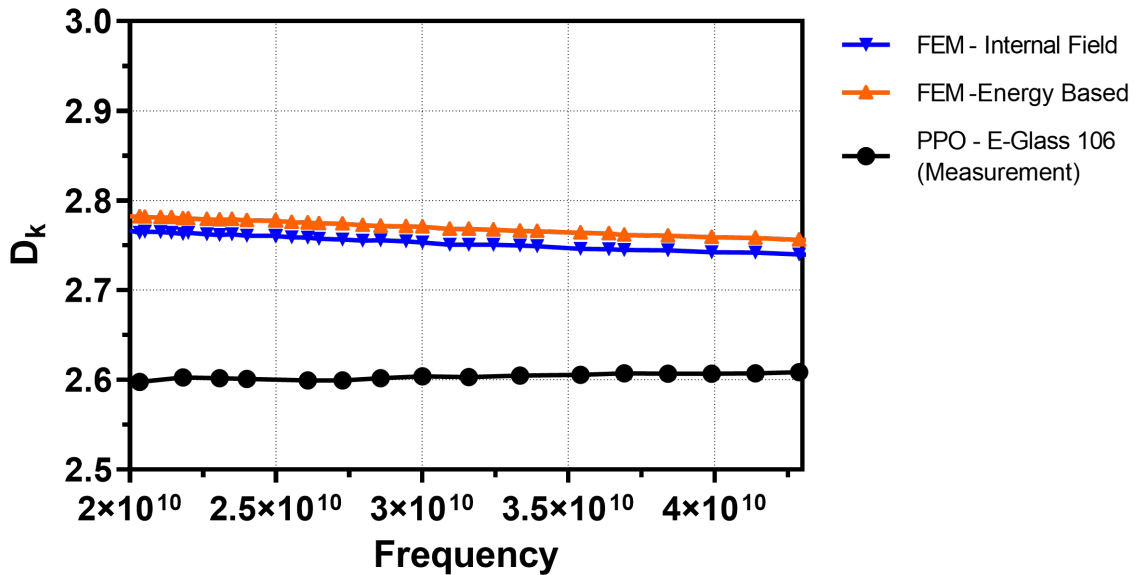


Figure 4.3: E-Glass(106) reinforced PPO based composite's single level homogenization based modelling compared with the measurement results of dielectric constant via FPOR between 20 GHz to 40 GHz

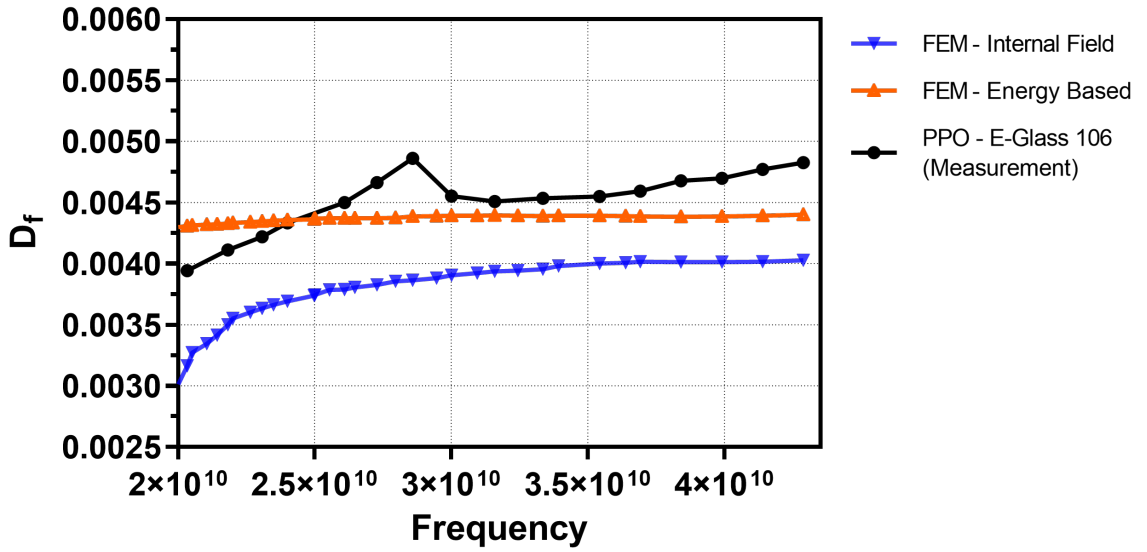


Figure 4.4: E-Glass(106) reinforced PPO based composite’s single level homogenization based modelling compared with the measurement results of dissipation factor via FPOR between 20 GHz to 40 GHz

Consequently, both the single and two-level homogenization procedures applied on the E-Glass(1080)+PPO composition and compared with the FPOR measurement results in between 20 GHz to 40 GHz. The simulation and measurement results are in good agreement among them. Whereas, extracted effective dissipation factor from the simulation environment underestimates the dissipation factor. As a result the extraction of effective dissipation factor by using internal field approach, the single level homogenization presents more accurate estimation in terms of FPOR measurement results.

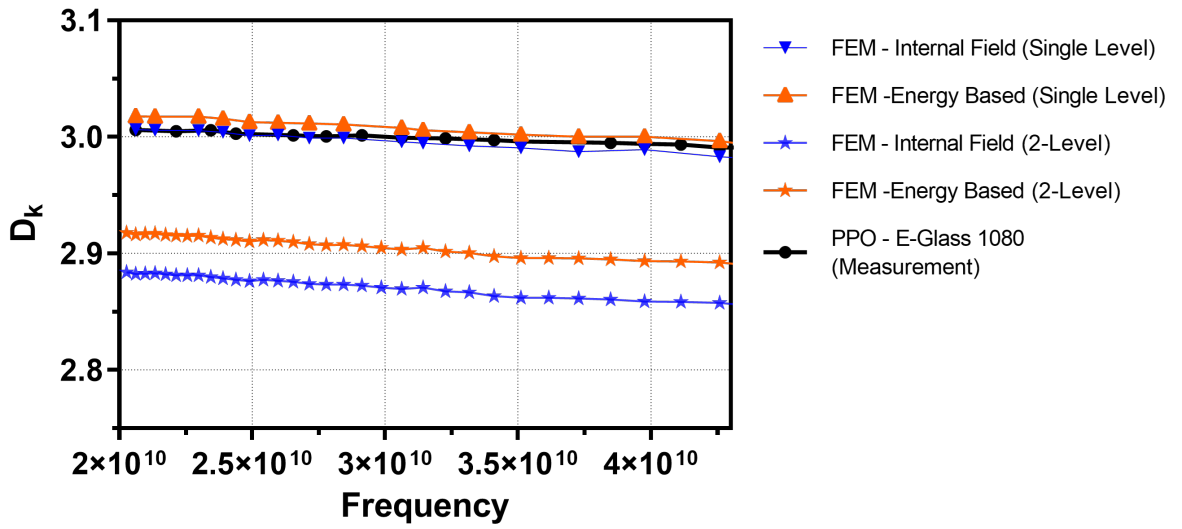


Figure 4.5: E-Glass(1080) reinforced PPO based composite's both single and two level homogenization based modelling compared with the measurement results of dielectric constant via FPOR between 20 GHz to 40 GHz

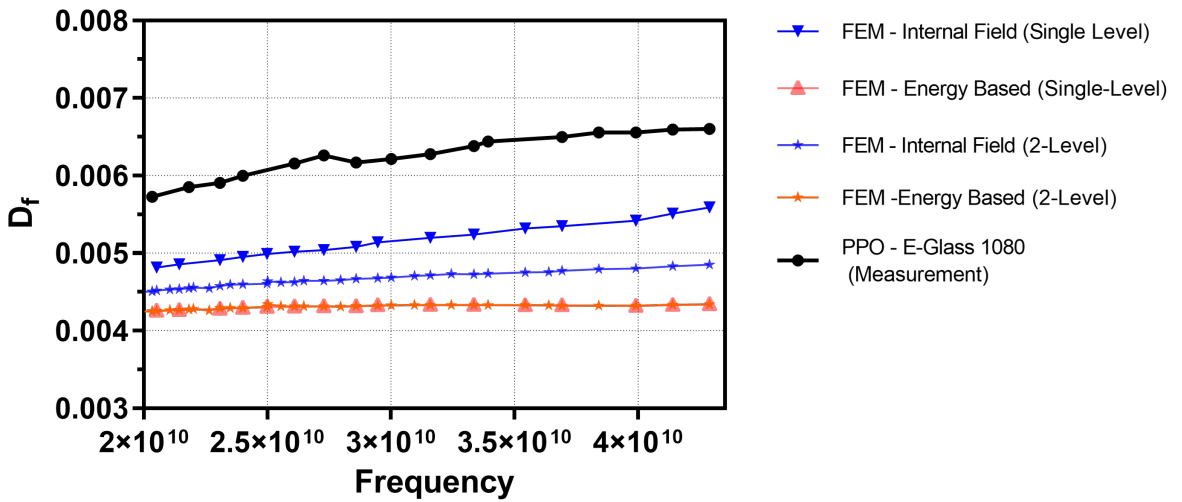


Figure 4.6: E-Glass(1080) reinforced PPO based composite's single and two level homogenization based modelling compared with the measurement results of dielectric constant via FPOR between 20 GHz to 40 GHz

4.1.1 FPOR Measurements of the Functionalized Reinforced Composites

In this study, except the modelling and the measurement procedures of the reinforced composites, reinforcement functionalization was also studied. Therefore, 106 and 1080 types of E-Glass fabrics were initially functionalized by three different silane coupling agents with amine, vinyl and epoxy end groups, in ethanol solutions. Therefore, the effect of functionalization of reinforcements on the effective dielectric properties of the composites were examined by using the FPOR measurements. As a result, obtained effective dielectric properties of the functionalized reinforced composites comprehensively explained in Appendix E.

4.2 Split Post Dielectric Resonator(SPDR) Measurement

Split post dielectric resonator (SPDR) is a type of resonator that operates in particularly determined frequency, this frequency also called as the nominal frequency. The nominal frequency of the current SPDR that utilized in this study is around 10.127 GHz. SPDR is one of the most precise dielectric properties measurement method which used for the measurement of laminar dielectric materials and LTCC substrates. The cross-sectional illustration and real measurement setup of the SPDR were presented in Figure 4.7 and Figure 4.8. The dielectric properties of the 106 and 1080 type reinforced composites SPDR measurements presented in Table 4.1. Consequently, the dielectric properties's measurement of the composites fabricated by using the functionalized reinforcements results presented in Appendix E.

Table 4.1: SPDR measurements of 106 and 1080 type reinforced PPO based composites at 10 GHz

Host matrix	E-Glass type	D_k	D_f
PPO	106	2.83	0.0039
PPO	1080	2.99	0.0042

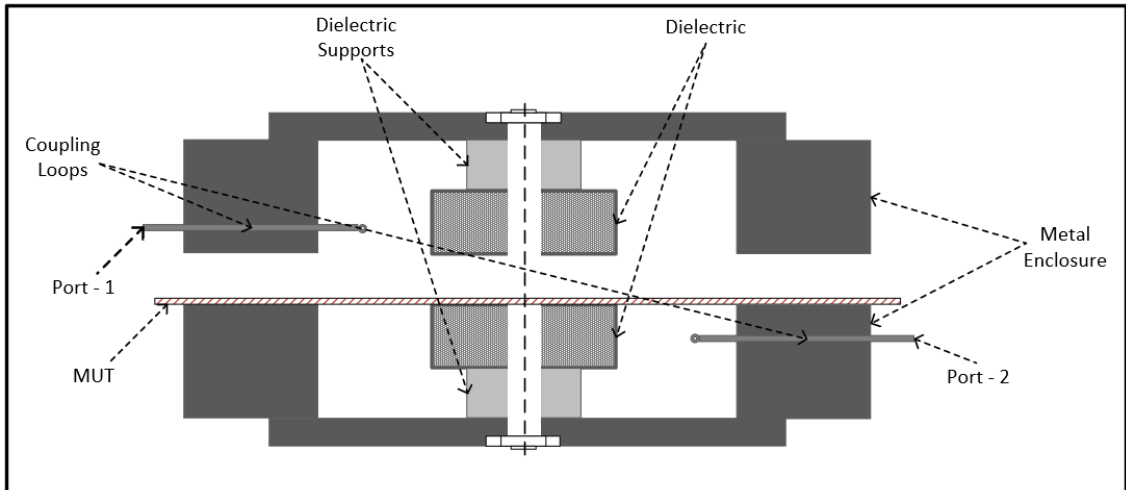


Figure 4.7: Cross-sectional illustration of the Split Post Dielectric Resonator.

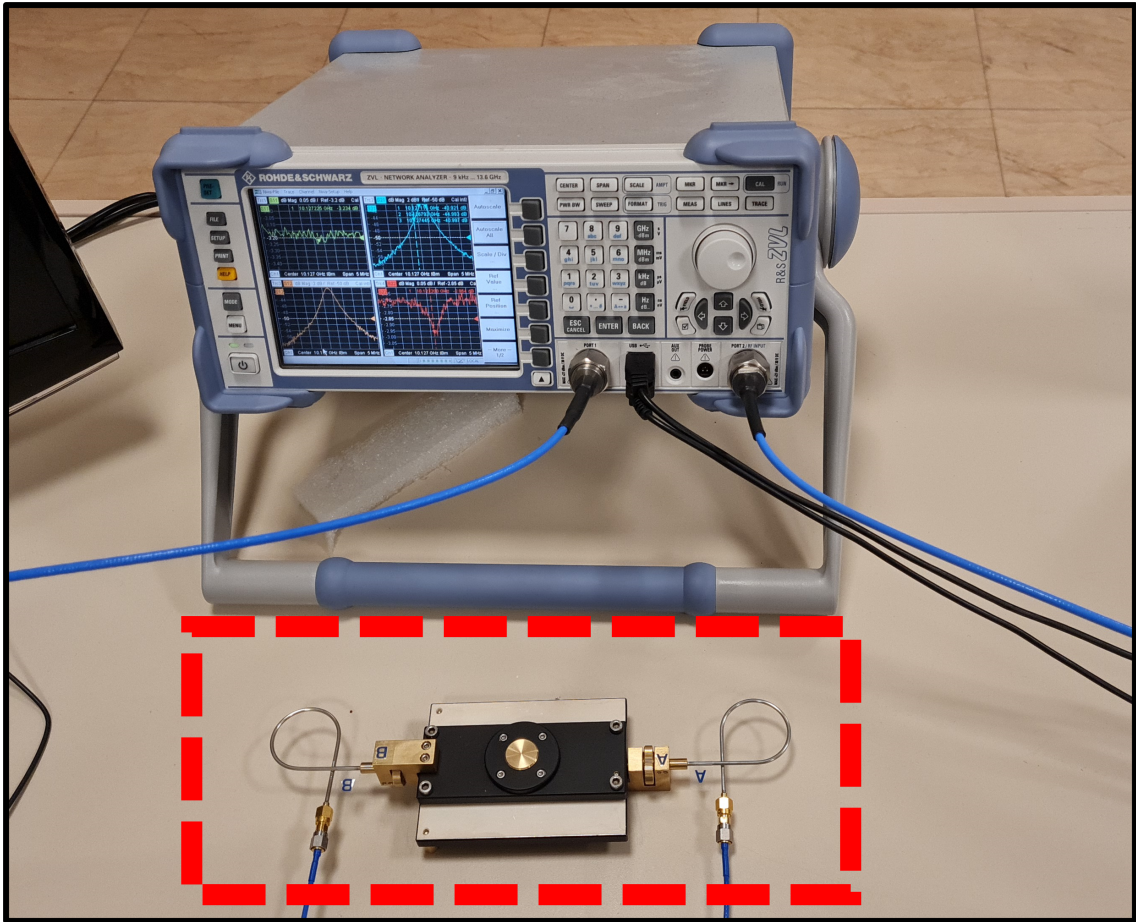


Figure 4.8: The realized measurement setup at 10 GHz for SPDR measurements.

4.3 Design of a Ring Resonator Measurement Setup

The micro-strip ring resonator structures have employed large variety of application in RF circuits. Therefore, in this study ring resonator structures can be utilized for the determination of the dielectric constant and the dissipation factor of the copper cladded composites [46]. The extraction procedure of the dielectric properties based on the quality factor and the resonance frequency of the MUT as similar to the FPOR and SPDR measurement techniques.

A micro-strip ring resonator designed to verify the extracted results from the SPDR measurement method at 10 GHz. In order to determine the dimensions of the circumference of the ring the guided wavelength has to be obtained as presented in equation (4.3.1).

$$\lambda_g = \frac{c}{f_0 \sqrt{|\varepsilon_{eff}|}} \quad (4.3.1)$$

where f_0 denotes resonance frequency, and ε_{eff} can be empirically calculated by the model provided by Kirschning et al. [47]. Whereas, in this design procedure the substrate selected arbitrarily and ε assumed as a bare PPO's complex permittivity. Calculation of 50 Ω matched micro-strip lines done by the line calculator in commercially available ADS software, which are used to couple the ring resonator. Furthermore the average radius of the, ring calculated via equation (4.3.2) [48].

$$2\pi r_{avg} = n\lambda_g \quad (4.3.2)$$

where n denotes the order of the harmonics and the r_{avg} denotes the average radius of the ring. The width of the ring accepted as same as the 50 Ω matched lines. Therefore, final layout of the ring resonator presented in Figure 4.9.

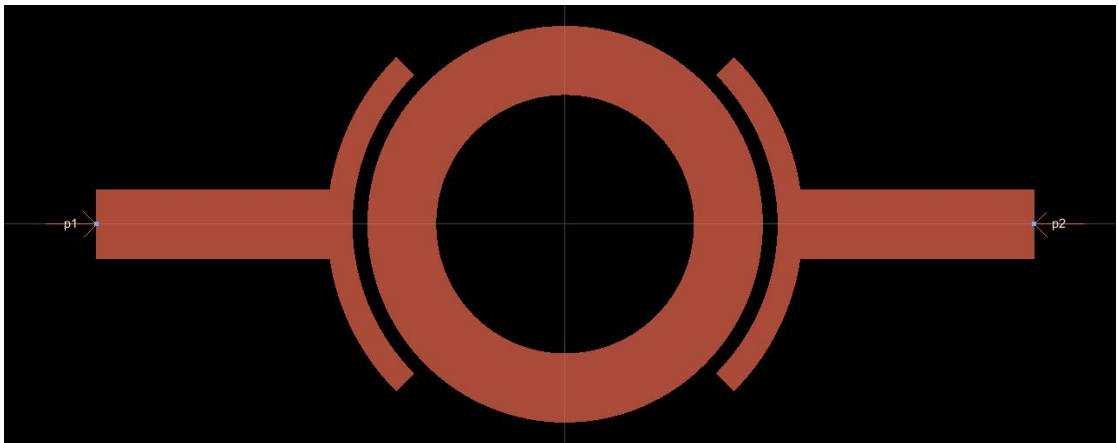


Figure 4.9: The layout of the designed micro-strip ring resonator in ADS on a arbitrarily defined substrate at 10 GHz

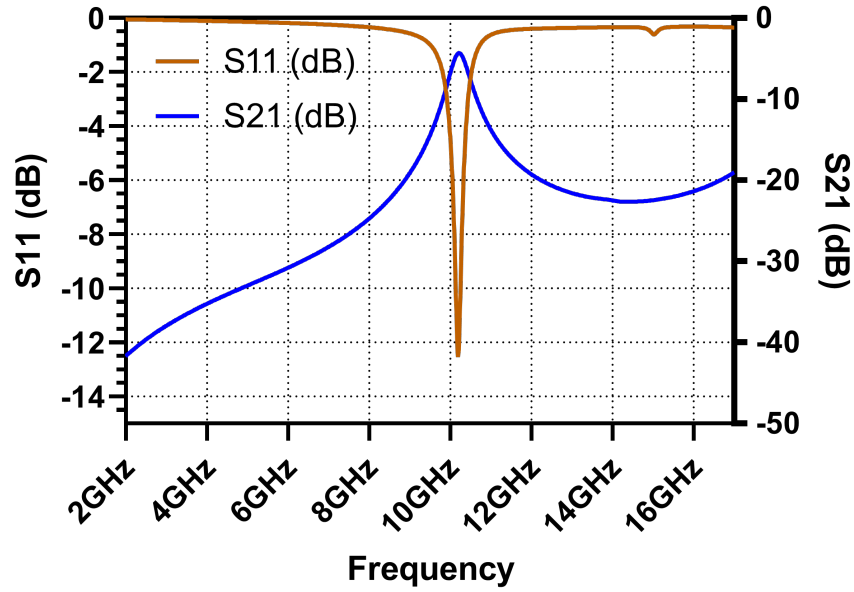


Figure 4.10: Extracted scattering parameters of the ring resonator from the ADS simulations

The EM simulations conducted by the commercially available ADS software and extracted S-parameters of the resonator presented in Figure 4.10. Therefore, the ring resonator is resonating at 10.22 GHz. In order to evaluate the SMA connectors effect on the board designed layout transferred into the COMSOL multi-physics environment and simulated via Electromagnetic waves module by introducing the transition boundary condition to express the coupling event. Subsequently, the designed resonator's electric field norm distribution at 10 GHz presented in Figure 4.11. Finally, extracted S-Parameters from COMSOL multi-physics simulations presented in Figure 4.12 and the resonance shifted to 9.8 GHz.

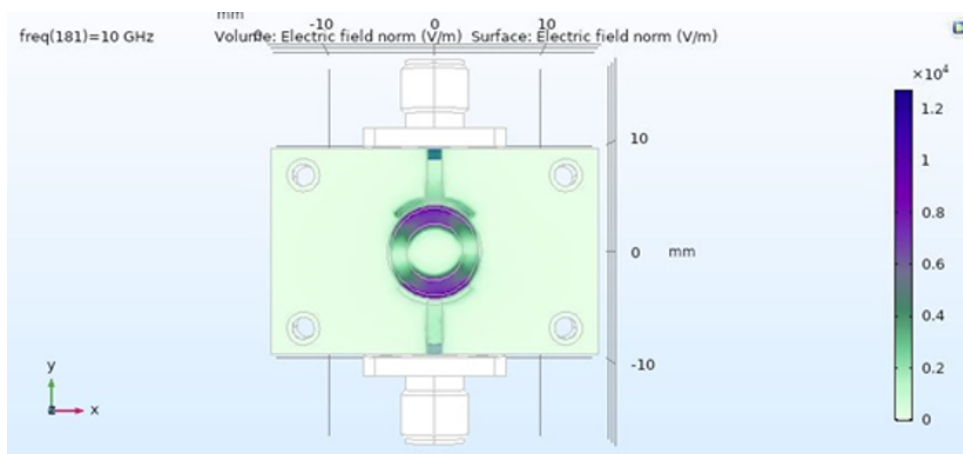


Figure 4.11: Designed micro-strip ring resonator simulation setup in COMSOL at 10 GHz

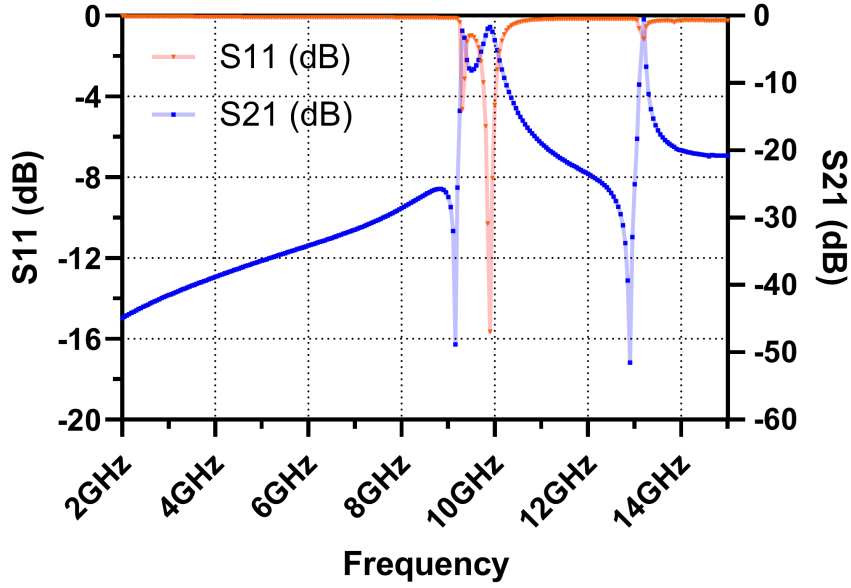


Figure 4.12: Extracted scattering parameters of the ring resonator from the COMSOL multi-physics simulations

As mentioned above, the calculation of dielectric properties depends on the resonance frequency and the quality factor. Whereas, measurement of the dielectric constant of a MUT more simple than the dissipation factor and can be measured by utilizing the equation (4.3.3) [48].

$$\varepsilon_r = \left(\frac{nc}{2\pi f_0} \right)^2 \quad (4.3.3)$$

Therefore, to measure the dissipation factor, it is required to extract the loaded quality factor (Q_L) and it can be calculated by the division of the resonance frequency to 3dB bandwidth of the insertion loss. Subsequently, the calculation of unloaded quality depends on the measurement of the insertion loss (IL) and it can be calculated as in equation (4.3.4) [48].

$$Q_0 = \frac{Q_L}{1 - 10^{-IL/20}} \quad (4.3.4)$$

Consequently, the quality factor of the dielectric losses dependent on the both unloaded quality factor and quality factor of the conductor loss as in presented in equation (4.3.5). The quality factor of the conductor losses described by the empirical methods proposed by S.B. Cohn et al. [48]. Therefore, $1/Q_d$ will describe the dissipation factor of the MUT.

$$D_f = \frac{1}{Q_d} = \frac{1}{Q_0} - \frac{1}{Q_c} \quad (4.3.5)$$

5 Conclusion & Future Work

5.1 Summary of Work

Copper cladded laminates have become a prominent material composition in electrical applications due to their superior electrical and mechanical properties. Primarily, low-loss laminates are one of the essential building blocks of the 5G applications due to the requirement of low attenuation in the signal line compared to the conventional epoxy-silica-based laminates. Predominantly vast majority of the integrated circuits are packed by silica blended epoxy structures due to the ease of processability and cost reduction. Therefore, wireless communications and broadband technologies are the primary motivation for developing advanced laminate systems with the enhanced dielectric properties. In these circumstances, the attention in the PCB substrates that operate at RF and mm-wave regions increases.

In this thesis, the modelling and the development of high performance, low-cost PCB substrate that operates in RF and mm-wave applications were performed. In order to achieve these specifications, we have examined the particular building blocks of the PCB laminates and determined the targeted chemical structures of the host matrix and the particular fiber weave structures. Due to the lack of prediction techniques of the laminates' mechanical and electrical properties, this study utilized two main approaches to determine the effective mechanical and electrical properties of a non-homogeneous laminate structure.

The internal field and the energy-based approaches were proposed to extract the effective electrical properties of a laminate. The obtained local dielectric properties of the laminate homogenized in the entire laminate system that infinitely repeats along the X and Y axis by using single and two-level homogenization procedures. The two-level homogenization procedure created an opportunity to simulate complex, multilayered laminates with a less computational load with respect to single-level homogenization.

The extracted effective complex permittivity of the laminates comprehensively were evaluated with the effective medium approximations. Thus, the average error rate of an effective dielectric constant between the Maxwell-Garnett approximation and the FEM-based internal field approach was around 1.8% at 40 GHz. On the other hand, the average error rate of an effective dissipation factor among the Maxwell-Garnett approximation and the FEM-based internal field approach was around 18.2% at 40 GHz.

Subsequently, modelled results were compared with the FPOR and SPDR measurements. 106 and 1080 types of reinforced PPO-based laminates were fabricated, and these samples have presented a good agreement with the proposed internal field and energy-based approaches. Thus, the average error rate of an effective dielectric constant between the FEM-based internal field approach and the measurements at 40 GHz was around 2.5%. On the other hand, the average error rate of an effective dissipation factor among the FEM-based internal field approach and the measurements at 40 GHz was around 19% at 40 GHz.

Finally, the fabricated samples were measured at the Ka-band and presented better performance than the common epoxy-silica-based composites in dielectric constant and dissipation factor. Consequently, at 10 GHz, the fabricated 1080 type reinforced laminate dielectric constant was 3, and the dissipation factor was 0.0042, which presents a magnitude of order less dissipation with respect to the FR-4 laminates. Consequently, we have examined surface functionalization of the reinforcements by treating various silane groups, and we obtained improvement on the effective dissipation factor of the laminate. These results are presented in Appendix E.

5.2 Future Work

There are two near future objectives of this study, initially, after the copper cladding procedure developed the ring resonator structure will be fabricated on top of a newly developed substrate and dielectric properties will be measured.

Secondly, as presented in the Appendix E, the preliminary results of functionalized reinforced PPO based composites shows that functionalization is promising in enhancing the current dielectric properties of the fabricated samples. However, due to the limited knowledge about the functionalized surface on the reinforcements the modelling of these composites have not been completed. To model these inclusions into the modeling environment, detailed characterization of the E-Glass is necessary such as thickness and uniformity of the functionalized layer and the determination of the complex permittivity. The long-term future work of this study is the further development of mechanical and thermal models of the laminates. Subsequently, the merging procedure of the mechanical and electromagnetic simulations will be done in a single platform to extract the effective dielectric and mechanical properties in a coupled way.

APPENDIX

A. Appendix

```
clear;
clc;
er_inf = 2.501;
er_dc = 2.617;
omg = 500*2*pi;
Tau_0 = 0.5e-12;
act = 9.65e-20;
act2 = 8.65e-20;
act3 = 7.65e-20;
T = (210:1:500);
tau = Tau_0 * exp(act./((1.38E - 23) * T));
er = 2.501 + ((2.617 - 2.501)./(1 + (omg * tau).^2));
T2 = (210 : 1 : 500);
tau2 = Tau_0 * exp(act2./((1.38E - 23) * T2));
er2 = 2.501 + ((2.617 - 2.501)./(1 + (omg * tau2).^2));
T3 = (210 : 1 : 500);
tau3 = Tau_0 * exp(act3./((1.38E - 23) * T3));
er3 = 2.501 + ((2.617 - 2.501)./(1 + (omg * tau3).^2));
figure(3);
plot(T, er);
hold on
plot(T, er2);
plot(T, er3);
grid on;
legend('tau_0 = 9.65E - 20', 'tau_0 = 8.65E - 20', 'tau_0 = 7.65E - 20', 'Location', 'southeast')
hold off
xlabel('Temperature(Kelvin)', 'FontSize', 14, 'FontWeight', 'b');
ylabel('Permittivity(Real)', 'FontSize', 14, 'FontWeight', 'b');
```

B. Appendix

```
clear;
clc;
er_inf = 0.011202587051851;
er_dc = 0.00176059026192027;
omg = 500*2*pi;
Tau_0 = 0.5e-12;
act = 9.65e-20;
act2 = 8.65e-20;
act3 = 7.65e-20;
T = (210:1:500);
tau = Tau_0.*exp(act./((1.38E-23).*T));
er = ((omg.*tau).*(er_dc - er_inf))./(1+(omg.*tau).^2);
T2 = (210 : 1 : 500);
tau2 = Tau_0.*exp(act2./((1.38E - 23). * T2));
er2 = ((omg.*tau2).*(er_dc - er_inf))./(1 + (omg.*tau2).^2);
T3 = (210 : 1 : 500);
tau3 = Tau_0.*exp(act3./((1.38E - 23). * T3));
er3 = ((omg.*tau3).*(er_dc - er_inf))./(1 + (omg.*tau3).^2);
figure(4);
plot(T, abs(er));
hold on
plot(T, abs(er2));
plot(T, abs(er3));
grid on;
legend('tau_0 = 9.65E - 20', 'tau_0 = 8.65E - 20', 'tau_0 = 7.65E - 20', 'Location', 'northeast')
hold off
xlabel('Temperature(Kelvin)', 'FontSize', 14, 'FontWeight', 'b');
ylabel('Permittivity(Imaginary)', 'FontSize', 14, 'FontWeight', 'b');
```

C. Appendix

```

clc;
clear;
last= 15;
epsilon_i =0.0039;
f=0.185;
A= 2;
epsilon_h=csvread('A:
umut data
eh_20GHz.csv',0,0,[0 0 last 0]);
%Maxwell-Garnett
for i=1:last+1
epsilon_eff(i,1) = epsilon_h(i,1) + 3*f*epsilon_h(i,1)*
((epsilon_i-epsilon_h(i,1))/(epsilon_i+2*epsilon_h(i,1)));
end
% Symmetric Bruggeman Approx.
for i=1:last+1
epsilon_eff_SBA(i,1) = (1/4)*(3*f*(epsilon_i-epsilon_h(i,1)) + 2*epsilon_h(i,1)-epsilon_i
+ ...
sqrt((1-3*f^2)*epsilon_i^2 + 2*(2+9*f-9*f^2)*epsilon_i*epsilon_h(i,1)+((3*f-2)^2)*(epsilon_h(i,1))^2
));
end
%Looyenga Approx.
for i=1:last+1
epsilon_eff_LA(i,1) = (((epsilon_i)^(1/A)-(epsilon_h(i,1))^(1/A))*f+(epsilon_h(i,1))^(1/A))^A;
end

```

D. Appendix

```
clc;
clear;
last= 47;
epsilon_0 = 8.854e - 12;
Weav = csvread('A : data_1energy.csv', 0, 0, [00last0]);
NormE = csvread('A : data_1energy.csv', 0, 1, [01last1]);
Qe = csvread('A : data_1energy.csv', 0, 2, [02last2]);
freq = csvread('A : data_1energy.csv', 0, 4, [04last4]);

for i=1:last+1
epsilon_double_prime(i,1) =(2*Qe(i,1))/(epsilon_0* 2*pi*freq(i,1)*(NormE(i,1))^2);
end
fori = 1 : last + 1
epsilon_single_prime(i, 1) = (4 * Weav(i, 1))/(epsilon_0 * (NormE(i, 1))^2);
end
fori = 1 : last + 1
Df_mtd_1(i, 1) = epsilon_double_prime(i, 1)/epsilon_single_prime(i, 1);
end

Dy =csvread('A:data_2_internal_energy.csv',0,0,[0 0 last 0]);
Ey =csvread('A:data_2_internal_energy.csv',0,1,[0 1 last 1]);
for i=1:last+1
epsilon(i,1) = Dy(i,1)/(Ey(i,1)*epsilon_0);
end
epsilon_single_prime_method2 = real(epsilon);
epsilon_double_prime_method2 = imag(epsilon);
for i=1:last+1
Df_mtd_2(i,1)= abs (epsilon_double_prime_method2(i,1)/epsilon_single_prime_method2(i,1));
end
```

E. Appendix

FPOR measurements of the functionalized reinforced composites

As mentioned in characterization part, to decrease effective dissipation factor of the 106 and 1080 type reinforced composite structures, we have functionalized the 106 and 1080 type E-Glass. To provide better bonding with the host matrix (PPO), E-glass surfaces were functionalized with silane coupling agents. Silane solutions were prepared in ethanol. 0.1%, 1% and 1% solutions of APTES, VTES and, GPTES, respectively, were prepared by weight.

Solutions were poured into containers and E-glass fabrics were soaked in the solutions for 48 hours. Then, they were dried at room temperature to evaporate excess ethanol. Vinyl ends of VTES can be involved in the polymerization of the resin by reacting with the vinyl end groups of the PPO-based resin during the curing procedure. The presence of the peroxide initiator in the reaction system will create viable conditions for polymerization to occur between the vinyl groups attached on the E-glass surface and the vinyl groups of the PPO-based host matrix. As a result the bonding between host matrix and E-Glass inclusions can be improved which, effectively increases the GTRR in unit volume of the composite. Therefore, to examine the GTRR in a laminate, we have examined the cross sectional image of the structure via SEM images. Figure 5.2 presented the control group which was manufactured with PPO based resin and untreated 1080 type reinforcement. Thus, Figure 5.3 presented the functionalized reinforcement via vinyl groups (VTES). Figures 5.2 and 5.3 were presenting the indications of GTRR has altered by the functionalization procedure. Subsequently, in Figure 5.1a 106 type and in Figure 5.1b 1080 type functionalized composites are examined in terms of effective dielectric constant and dissipation factor. Finally, SPDR measurement versions of the functionalized reinforced composites results presented in Table 5.1.

Table 5.1: SPDR measurements of 106 and 1080 type functionalized reinforced PPO based composites at 10 GHz

Sample name	Silane Type	Host matrix	E-Glass type	D_k	D_f
PPO-106-C	Control	PPO	106	2.83	0.0039
PPO-1080-C	Control	PPO	1080	2.99	0.0042
PPO-106-A	APTES	PPO	106	2.46	0.0038
PPO-1080-A	APTES	PPO	1080	2.87	0.0047
PPO-106-V	VTES	PPO	106	2.72	0.0036
PPO-1080-V	VTES	PPO	1080	2.84	0.0042
PPO-106-E	GPTES	PPO	106	2.48	0.0037
PPO-1080-E	GPTES	PPO	1080	2.69	0.0043

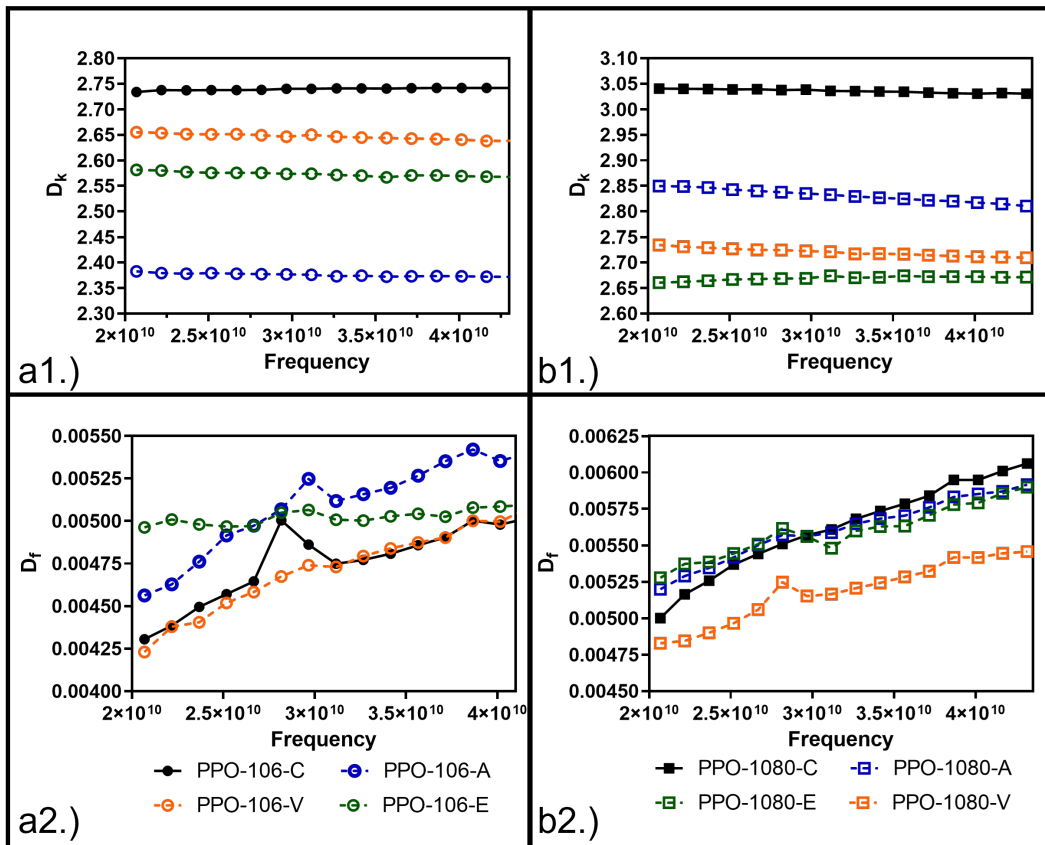


Figure 5.1: The effective dielectric properties measurements of the functionalized reinforcements as function of frequency. a.) Experiment set with functionalized E-Glass(106)+PPO, b.) Experiment set with functionalized E-Glass(1080)+PPO

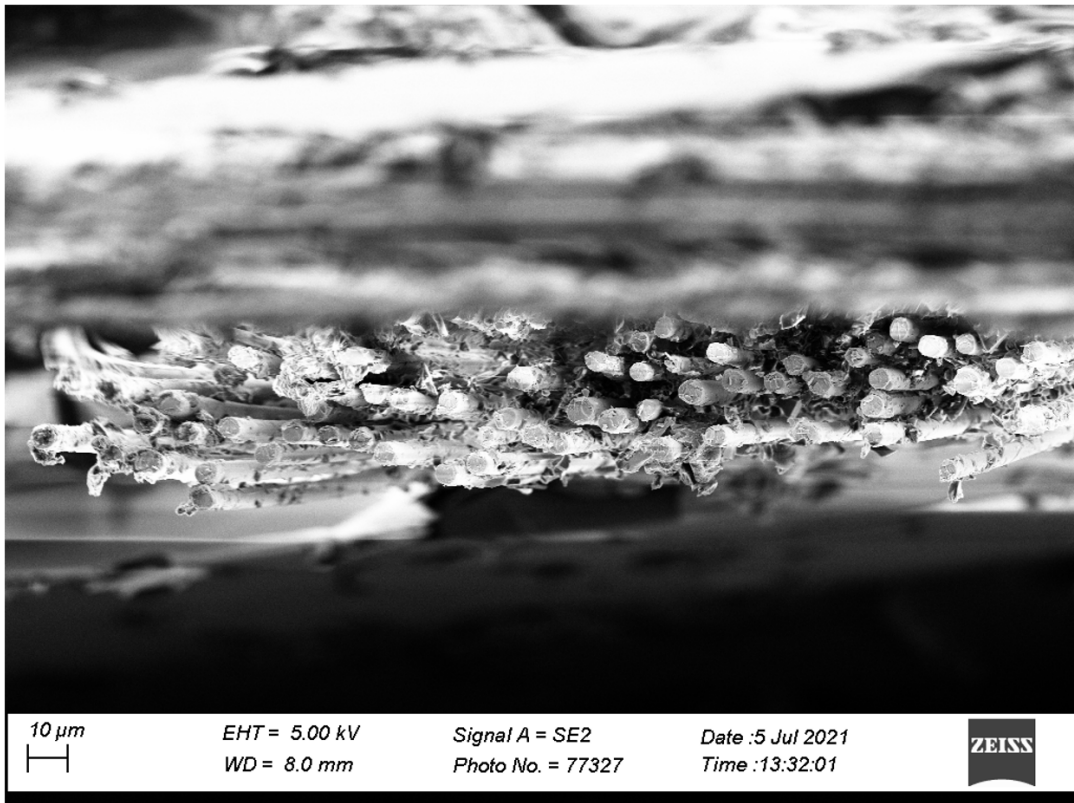


Figure 5.2: Cross-sectional SEM image of an untreated 1080 type E-Glass with PPO based composite.

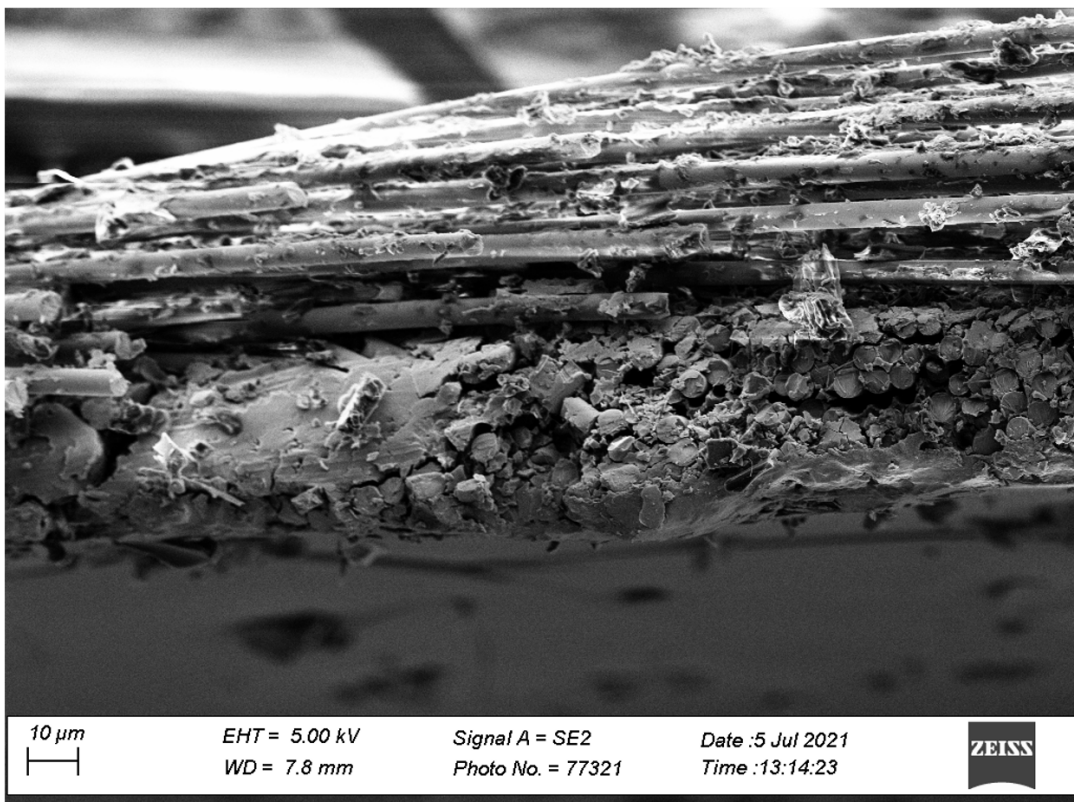


Figure 5.3: Cross-sectional SEM image of an vinylsilane (VTES) treated 1080 type E-Glass with PPO based composite.

References

- [1] C. A. Balanis, *Antenna theory: Analysis and design*. Wiley, 2016.
- [2] R. Ludwig and P. Bretchko, *Rf circuit design: Theory and applications*. Prentice-Hall, 2000.
- [3] J. Sharma, M. Choate, and S. P. Isola, “Laminate materials with low dielectric properties,” 2002.
- [4] J. Baker-Jarvis, M. Janezic, B. Riddle, C. Holloway, N. Paulter, and J. Blendell, “Dielectric and conductor-loss characterization and measurements on electronic packaging materials,” 2001-07-01 2001.
- [5] Y. Cheng, X. Chen, K. Wu, S. Wu, Y. Chen, and Y. Meng, “Modeling and simulation for effective permittivity of two-phase disordered composites,” *Journal of Applied Physics*, vol. 103, no. 3, p. 034111, 2008.
- [6] E. Tuncer, S. M. Gubański, and B. Nettelblad, “Dielectric relaxation in dielectric mixtures: Application of the finite element method and its comparison with dielectric mixture formulas,” *Journal of Applied Physics*, vol. 89, no. 12, pp. 8092–8100, 2001.
- [7] N. Jebbor and S. Bri, “Effective permittivity of periodic composite materials: Numerical modeling by the finite element method,” *Journal of Electrostatics*, vol. 70, no. 4, pp. 393–399, 2012.
- [8] H. Li, D. Eng, C. Tang, and P. Westbrook, “Low dielectric glass fibre development - new printed circuit board base materials,” *Glass Technology: European Journal of Glass Science and Technology Part A*, vol. 54, pp. 81–85, 04 2013.
- [9] E. Tuncer, Y. Serdyuk, and S. Gubanski, “Dielectric mixtures: electrical properties and modeling,” *IEEE Transactions on Dielectrics and Electrical Insulation*, vol. 9, no. 5, pp. 809–828, 2002.
- [10] E. Tuncer, B. Nettelblad, and S. M. Gubański, “Non-debye dielectric relaxation in binary dielectric mixtures (50-50): Randomness and regularity in mixture topology,” *Journal of Applied Physics*, vol. 92, no. 8, pp. 4612–4624, 2002.
- [11] E. Tuncer and S. M. Gubanski, “Dielectric properties of different composite structures,” in *Polymers and Liquid Crystals* (A. Wlochowicz, ed.), vol. 4017, pp. 136 – 142, International Society for Optics and Photonics, SPIE, 1999.
- [12] D. M. Pozar, *Microwave engineering / David M. Pozar, University of Massachusetts at Amherst*. Wiley, 2012.
- [13] F. T. Ulaby and U. Ravaioli, *Fundamentals of applied electromagnetics*. Pearson, 2015.
- [14] S. P. Simmons, *Electromagnetic analysis of heterogeneous woven fabric composite laminates*. PhD thesis, University of Delaware, 2019.

- [15] S. Kasap, *Principles of Electronic Materials and Devices*. USA: McGraw-Hill, Inc., 3 ed., 2005.
- [16] R. Corporation, “Practical measurements of dielectric constant and loss for pcb materials at high frequency,” 2014.
- [17] R. M. Mimoso, *Multiscale method for the calculation of effective dielectric properties*. PhD thesis, Tecnico Lisboa, 2014.
- [18] L. Gunther, *Electromagnetic Field Theory for Engineers and Physicists*. Springer Berlin Heidelberg, 2010.
- [19] L. F. Chen, *Microwave electronics: measurement and materials characterisation*. Wiley, 2004.
- [20] D. Prastiyanto, *Temperature- and Time-Dependent Dielectric Measurements and Modelling on Curing of Polymer Composites*. PhD thesis.
- [21] S. Mumby, “An overview of laminate materials with enhanced dielectric properties,” *Journal of Electronic Materials*, vol. 18, pp. 241–250, 01 1989.
- [22] IPC-TA-720, “Technology assessment of laminates,” p. Article 5.1, 1987.
- [23] P. Cassidy, *Thermally stable polymers: syntheses and properties*. Dekker, 1980.
- [24] W. Chen, H. Yang, H. Zou, and P. Liu, “Compatibilized the thermosetting blend of epoxy and redistributed low molecular weight poly(phenylene oxide) with triallylisocyanurate,” *Journal of Applied Polymer Science*, vol. 133, no. 20, 2016.
- [25] H.-J. Hwang, S.-W. Hsu, and C.-S. Wang, “Synthesis and physical properties of low-molecular-weight redistributed poly(2,6-dimethyl-1,4-phenylene oxide) for epoxy resin,” *Journal of Applied Polymer Science*, vol. 110, no. 3, p. 1880–1890, 2008.
- [26] H.-J. Hwang, S.-W. Hsu, C.-L. Chung, and C.-S. Wang, “Low dielectric epoxy resins from dicyclopentadiene-containing poly(phenylene oxide) novolac cured with dicyclopentadiene containing epoxy,” *Reactive and Functional Polymers*, vol. 68, no. 8, p. 1185–1193, 2008.
- [27] L. Wang, C. Liu, S. Shen, M. Xu, and X. Liu, “Low dielectric constant polymers for high speed communication network,” *Advanced Industrial and Engineering Polymer Research*, vol. 3, no. 4, p. 138–148, 2020.
- [28] A. Rusli, W. D. Cook, T. L. Schiller, and K. Saito, “Blends of epoxy-amine resins with poly(phenylene oxide) as processing aids and toughening agents: I. uncured systems,” *Polymer International*, vol. 63, no. 1, p. 52–59, 2013.
- [29] J. P. Calame, A. Birman, Y. Carmel, D. Gershon, B. Levush, A. A. Sorokin, V. E. Semenov, D. Dadon, L. P. Martin, M. Rosen, and et al., “A dielectric mixing law for porous ceramics based on fractal boundaries,” *Journal of Applied Physics*, vol. 80, no. 7, p. 3992–4000, 1996.

- [30] J. Peón-Fernández, M.-H. J., N. Banerji, and T. Iglesias, “Numerical study of effective permittivity in composite systems,” *Applied Surface Science*, vol. 226, no. 1-3, p. 78–82, 2004.
- [31] D. R. Smith, S. Schultz, P. Markoš, and C. M. Soukoulis, “Determination of effective permittivity and permeability of metamaterials from reflection and transmission coefficients,” *Physical Review B*, vol. 65, no. 19, 2002.
- [32] O. Acher, J.-M. Lerat, and N. Malléjac, “Evaluation and illustration of the properties of metamaterials using field summation,” *Optics Express*, vol. 15, no. 3, p. 1096, 2007.
- [33] P. Gonon, A. Sylvestre, J. Teyseyre, and C. Prior *Journal of Materials Science: Materials in Electronics*, vol. 12, no. 2, p. 81–86, 2001.
- [34] C. Brosseau and A. Beroual, “Computational electromagnetics and the rational design of new dielectric heterostructures,” *Progress in Materials Science*, vol. 48, no. 5, p. 373–456, 2003.
- [35] B. Sareni, L. Krähenbühl, A. Beroual, and C. Brosseau, “Ab initio simulation approach for calculating the effective dielectric constant of composite materials,” *Journal of Electrostatics*, vol. 40-41, 1997.
- [36] I. Krakovský and V. Myroshnychenko, “Modeling dielectric properties of composites by finite-element method,” *Journal of Applied Physics*, vol. 92, no. 11, p. 6743–6748, 2002.
- [37] V. Myroshnychenko and C. Brosseau, “Effective complex permittivity and continuum percolation analysis of two-phase composite media,” *IEEE Transactions on Dielectrics and Electrical Insulation*, vol. 16, no. 4, p. 1209–1222, 2009.
- [38] V. Myroshnychenko and C. Brosseau, “Analysis of the effective permittivity in percolative composites using finite element calculations,” *Physica B: Condensed Matter*, vol. 405, no. 14, p. 3046–3049, 2010.
- [39] T. Weiland, R. Schuhmann, R. B. Gregor, C. G. Parazzoli, A. M. Vetter, D. R. Smith, D. C. Vier, and S. Schultz, “Ab initio numerical simulation of left-handed metamaterials: Comparison of calculations and experiments,” *Journal of Applied Physics*, vol. 90, no. 10, p. 5419–5424, 2001.
- [40] L. Liu, S. M. Matitsine, Y. B. Gan, and K. N. Rozanov, “Effective permittivity of planar composites with randomly or periodically distributed conducting fibers,” *Journal of Applied Physics*, vol. 98, no. 6, p. 063512, 2005.
- [41] R. Mekala and N. Badi, “Modeling and simulation of high permittivity core-shell ferroelectric polymers for energy storage solutions,” 2013.
- [42] E. Tuncer, “Dielectric mixtures-importance and theoretical approaches,” *IEEE Electrical Insulation Magazine*, vol. 29, no. 6, pp. 49–58, 2013.
- [43] G. Girard, M. Jrad, S. Bahi, M. Martiny, S. Mercier, L. Bodin, D. Nevo, and S. Dareys, “Experimental and numerical characterization of thin woven composites used in printed circuit boards for high frequency applications,” *Composite Structures*, vol. 193, pp. 140–153, 2018.

- [44] G. P. STEVEN, “Homogenization of multicomponent composite orthotropic materials using fea,” *Communications in Numerical Methods in Engineering*, vol. 13, no. 7, p. 517–531, 1997.
- [45] T. Karpisz, B. Salski, P. Kopyt, and J. Krupka, “Measurement of dielectrics from 20 to 50 ghz with a fabry–pérot open resonator,” *IEEE Transactions on Microwave Theory and Techniques*, vol. 67, no. 5, p. 1901–1908, 2019.
- [46] J.-M. Heinola, P. Silventoinen, K. Latti, M. Kettunen, and J.-P. Strom, “Determination of dielectric constant and dissipation factor of a printed circuit board material using a microstrip ring resonator structure,” in *15th International Conference on Microwaves, Radar and Wireless Communications (IEEE Cat. No.04EX824)*, vol. 1, pp. 202–205 Vol.1, 2004.
- [47] M. Kirschning and R. Jansen, “Accurate model for effective dielectric constant of microstrip with validity up to millimetre-wave frequencies,” *Electronics Letters*, vol. 18, no. 6, p. 272, 1982.
- [48] J.-M. Heinola, K.-P. Latti, J.-P. Strom, M. Kettunen, and P. Silventoinen, “A strip line ring resonator method for determination of dielectric properties of printed circuit board material in function of frequency,” in *The 17th Annual Meeting of the IEEE Lasers and Electro-Optics Society, 2004. LEOS 2004.*, pp. 692–695, 2004.